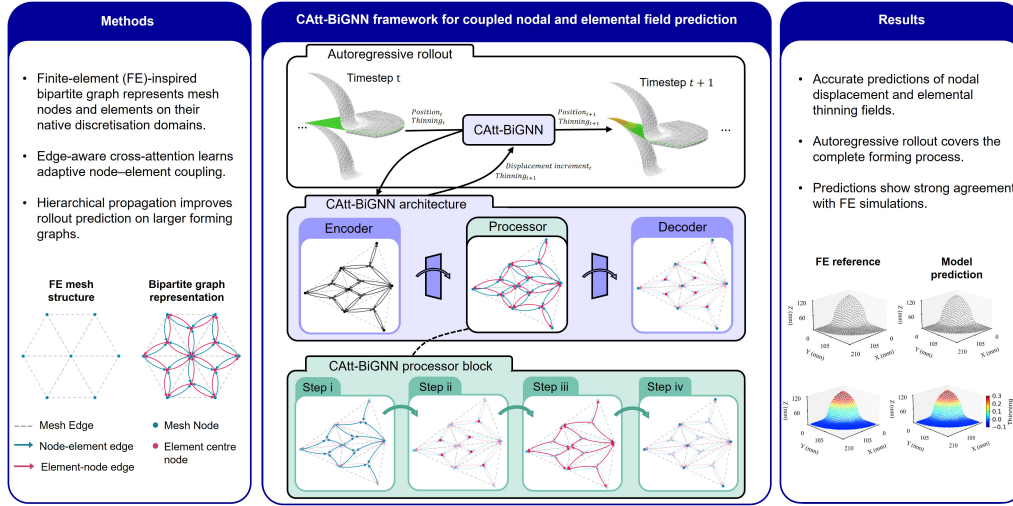


Graphical Abstract

A finite-element-inspired bipartite graph learned simulator for manufacturability assessment in large-deformation sheet forming

Yingxue Zhao, Haoran Li, Haosu Zhou, Tobias Pfaff, Nan Li



A finite-element-inspired bipartite graph learned simulator for manufacturability assessment in large-deformation sheet forming

Yingxue Zhao^a, Haoran Li^a, Haosu Zhou^a, Tobias Pfaff^b, Nan Li^{a,*}

^a*Dyson School of Design Engineering, Imperial College London, London, UK*

^b*NVIDIA, UK*

Abstract

Explicit dynamic finite element (FE) simulations are widely used for large-deformation engineering analysis, but iterative simulations remain expensive in design-space exploration and optimisation. In explicit FE analysis, nodal kinematics and element-level deformation measures evolve through a coupled node–element update process. This motivates graph learned simulators that approximate one-step FE state transitions and roll them out autoregressively. However, many mesh-based graph surrogates remain node-centred, so element-level variables and native nodal-elemental exchange relations are less directly represented in the learned graph state. This work proposes CAtt-BiGNN, a cross-attention-based bipartite graph neural network for coupled nodal–elemental learning. The bipartite graph provides a finite-element-inspired representation of FE entities and exchange relations. FE mesh nodes and elements are represented as distinct graph entities connected by directed node–element edges, enabling nodal displacement increments and element-level deformation states to be predicted on their native discretisation domains. An edge-aware cross-attention processor uses geometric edge embeddings to adaptively modulate directional node–element message passing. For larger graphs, CAtt-BiUGNN combines the bipartite processor with bipartite graph downsampling and upsampling to enhance long-range information propagation. The method is evaluated on dome-shaped cold-forming and corner-shaped hot-forming benchmarks. Comparisons with node-centred baselines, bipartite and attention ablations show that the proposed models

*Corresponding author. E-mail address: n.li09@imperial.ac.uk (N. Li)

improve the accuracy and balance of nodal displacement and elemental thinning prediction during autoregressive rollout. The proposed finite-element-inspired learned simulator improves manufacturability-oriented nodal and elemental field prediction and can support efficient design-space exploration in large-deformation sheet material forming.

Keywords: Sheet material forming, Finite-element-inspired graph learning, Bipartite graph, Cross-attention mechanism, Hierarchical graph neural network, Manufacturability-oriented field prediction

1. Introduction

Explicit dynamic finite element (FE) simulations are widely used for large-deformation engineering analysis [1–3]. They provide detailed predictions of nodal kinematics and element-level deformation measures, including displacement, strain, stress, and thickness variation [1, 2, 4, 5]. In an explicit dynamic FE formulation, the simulation advances the mesh state step by step. Nodal displacements drive the deformation of finite elements, while element-level quantities evaluated at integration points contribute back to nodal equilibrium through the assembly of internal forces. This coupled nodal-elemental update structure is important for predicting deformation behaviour, strain localisation, and failure-related phenomena in engineering applications. However, high-fidelity FE simulations remain computationally expensive when large design spaces are explored or when iterative optimisation is required [6–9].

Machine learning (ML)-based simulation models provide a promising route for accelerating FE analyses [10–14]. GNNs provide relational inductive biases for learning over entities and interactions [15–17]. They are particularly well suited to mesh-based simulations because they can operate directly on irregular discretisations and local mesh connectivity [18–20]. Rather than learning only a direct mapping from design variables to final response fields, a graph learned simulator can approximate the one-step update of the underlying numerical simulation and roll it out autoregressively over time [18, 19, 21, 22]. This setting is well matched to explicit dynamic FE analysis, where the physical state evolves through a sequence of local updates on a mesh. During rollout, the predicted state at one timestep becomes part of the input for the next timestep. This distinguishes graph learned simulators from static final-state regression models. GNN-based models have therefore

shown promising performance across a range of mechanics-related simulation and engineering prediction tasks [23–27].

Despite these advances, many existing mesh-based graph surrogates and learned simulators define the evolving graph state on a single type of mesh entity, most commonly mesh nodes [19, 21, 22, 26, 28, 29]. This representation is natural for nodal variables such as displacement, velocity, or acceleration. However, explicit FE simulations also contain quantities that are natively associated with elements or integration points, such as strain, stress, damage, or thinning [1–3, 5]. In applications such as sheet material forming, both nodal geometry evolution and element-level deformation indicators are relevant for manufacturability assessment [5, 30–32]. Representing these quantities through a single entity type is possible, but it often requires an additional mapping between nodal and elemental domains and can make the learned state less directly aligned with the native FE discretisation.

These considerations motivate a nodal-elemental graph state that reflects the native entity structure of the FE discretisation. Instead of collapsing nodal and elemental variables into a single node-centred graph state, the proposed representation retains mesh nodes and finite elements as distinct but coupled graph entities. Mesh-nodes store nodal kinematic and contact-related states, while element centre-nodes store element-level deformation states. Directed node-to-element and element-to-node edges define the interaction paths between the two domains and provide the basis for learning their coupling. This representation does not impose the FE equations explicitly. Instead, it provides a finite-element-inspired inductive bias by retaining the two FE entity types and allowing their exchange relations to be learned from simulation data.

A related line of work has adapted graph states and graph relations to the physical structure of specific engineering prediction tasks. In finite-element surrogate modelling, boundary-oriented graph embedding has been used to incorporate boundary, loading, and neighbouring-element information into graph construction for rapid field prediction in boundary-value problems [33]. In sheet-forming surrogate modelling, multi-level graph architectures and spatial-weighted graph convolutions have been used to improve high-fidelity forming-field prediction [34]. Hierarchical graph architectures have also been explored for mesh-based simulations to improve information propagation over larger computational domains [35]. In structural response prediction, physics-informed graph architectures have constructed adjacency relations from structural mechanics to encode physically meaningful sensor de-

dependencies [36]. In structural form-finding, graph learning frameworks have further incorporated domain-specific topology diagrams and validity rules into the learning process [37]. These studies show that engineering graph learning benefits when the graph state, graph relations, and learning architecture are aligned with the target physical problem. However, these methods are not primarily designed for coupled explicit-FE rollout in which nodal geometry evolution and element-level deformation states are represented on different discretisation domains and updated within a single learned simulation process. This motivates the nodal-elemental bipartite design adopted in this work.

Another line of work has connected graph learning more directly with numerical discretisation. Finite-volume-informed graph networks incorporate finite-volume constraints and discretisation-inspired aggregation schemes to improve prediction on unstructured flow grids [38]. Finite-element-inspired hypergraph neural networks further encode element-node connectivity by representing each finite element as a hyperedge linking its associated nodes [39]. These approaches strengthen the link between graph learning and numerical discretisation by using numerical schemes as architectural inductive biases. Nevertheless, the large-deformation sheet material forming problem considered in this work involves the coupled evolution of nodal kinematics and element-level deformation states, including thinning, within an autoregressive rollout setting. The present work therefore differs from existing discretisation-inspired graph models by treating finite elements as state-carrying graph entities and by learning bidirectional node-element updates within a single rollout process.

This work proposes CAtt-BiGNN, a cross-attention-based bipartite graph neural network designed to learn coupled nodal-elemental updates in explicit dynamic FE simulations. The proposed graph contains two types of graph entities: mesh-nodes and element centre-nodes. Mesh-nodes represent nodal states, while element centre-nodes represent element-level deformation states. Directed node-to-element and element-to-node edges connect each finite element to its associated mesh nodes. This construction is finite-element-inspired in the sense that it follows the native node-element structure of the discretisation, while the model remains a learned surrogate rather than an explicitly constrained finite-element solver. The bipartite representation allows nodal displacement increments and element-level deformation states to be predicted on their native discretisation domains. In the sheet material forming application studied in this paper, the element-level state is instantiated

as elemental thinning.

The core processor of CAtt-BiGNN uses an edge-aware cross-attention mechanism to learn directional node-element coupling. In the proposed attention design, the receiver state defines the query, the directed edge embedding defines the key, and the updated directed edge feature provides the message to be aggregated. This design differs from standard graph attention and conventional cross-attention because the attention weights are conditioned on geometric node-element relations. The model can therefore adapt the strength of node-element message passing according to local mesh geometry and deformation state. For larger graphs, a hierarchical extension, denoted CAtt-BiUGNN, combines the same bipartite processor with a graph down-sampling and up-sampling mechanism. This extension improves long-range information propagation while preserving the nodal-elemental representation across graph levels.

Large-deformation sheet material forming is used as the validation domain. Sheet material forming is widely used in the production of lightweight and high-strength components for automotive, aerospace, and energy applications [30]. Manufacturability assessment relies on accurate prediction of geometry evolution, strain localisation, and thickness variation, as these quantities are closely related to forming defects such as wrinkling, localised thinning, and fracture [31, 32]. In this work, the proposed models predict nodal displacement increments and elemental thinning fields during autoregressive rollout. The predicted displacement increments update the current geometry, and geometry-dependent graph features are recomputed before the next prediction step. This rollout setting allows the model to predict the progressive evolution of manufacturability-oriented fields rather than only the final forming response. The learned simulator therefore provides geometry and thinning fields for efficient comparison of candidate forming designs.

The proposed models are evaluated on two representative forming cases: a dome-shaped cold-forming case and a larger corner-shaped hot-forming case. These cases test the model under different graph sizes, geometric complexities, and forming conditions. The dome-shaped case is used to examine the effect of the bipartite representation and edge-aware cross-attention without hierarchical coarsening. The corner-shaped benchmark is used to evaluate the hierarchical CAtt-BiUGNN architecture under a more complex forming configuration with a larger graph and sharper geometric transitions. The evaluation includes comparisons with mesh-based node-centred baselines, bipartite ablation variants, attention variants, and a parameter-budget-controlled

comparison.

The main contributions of this work are summarised as follows.

- A finite-element-inspired bipartite graph representation is introduced for coupled nodal-elemental field prediction. Mesh nodes and finite elements are represented as distinct graph entities, allowing nodal displacement increments and element-level deformation states to be predicted on their native discretisation domains.
- An edge-aware cross-attention processor is developed to model directional node-element coupling. The attention weights are conditioned on geometric edge embeddings, enabling adaptive message passing according to local node-element relations.
- A hierarchical extension, CAtt-BiUGNN, is proposed for larger forming meshes. The downsampling and upsampling mechanism improves long-range information propagation while preserving the same bipartite node-element representation.
- The proposed models are evaluated through controlled ablation studies on cold- and hot-forming benchmarks, showing improved overall balance between nodal displacement prediction and elemental thinning prediction during autoregressive rollout for manufacturability-oriented field assessment.

The remainder of the paper is organised as follows. Section 2 reviews the node-element transfer pattern in the explicit finite element formulation and defines the surrogate prediction problem. Section 3 provides an overview of the proposed CAtt-BiGNN framework and its hierarchical extension. Section 4 describes the dataset generation procedure for the forming cases. Sections 5 and 6 present the bipartite graph representation and the proposed cross-attention-based bipartite graph neural network. Section 7 details the training, rollout, and adaptive Gaussian noise settings. Section 8 evaluates the proposed modelling choices through numerical comparisons and ablation studies, and Section 9 concludes the paper.

2. Explicit dynamic FE formulation and problem definition

Before introducing the bipartite graph representation in Section 5 and the model design in Section 6, this section reviews the explicit finite element (FE)

update cycle that motivates the proposed graph-based design. The focus is not to reproduce the full implementation of a commercial FE solver, but to identify the mesh entities and update dependencies that are relevant to the learned simulator. In particular, nodal kinematic updates are transferred through element connectivity to update element-level deformation measures, while updated element-level quantities contribute back to subsequent nodal dynamics through FE assembly. This coupled update pattern provides the modelling motivation for representing mesh nodes and finite elements as distinct but connected graph entities.

The following notation is used throughout this section. The position of node v at time t^n is denoted by \mathbf{x}_v^n , and its reference position is \mathbf{x}_v^0 . The accumulated nodal displacement and one-step displacement increment are defined as

$$\mathbf{u}_v^n = \mathbf{x}_v^n - \mathbf{x}_v^0, \quad \Delta \mathbf{u}_v^{n+1} = \mathbf{u}_v^{n+1} - \mathbf{u}_v^n = \mathbf{x}_v^{n+1} - \mathbf{x}_v^n. \quad (1)$$

Global vectors are written without the node subscript, for example \mathbf{u}^n and $\Delta \mathbf{u}^{n+1}$. The element index is denoted by i , and the integration-point index within element i is denoted by q . This distinction is important because stresses, strains, and thickness variables are generally evaluated at integration points, whereas the graph model later uses an element-level representation of these quantities.

2.1. Governing equation and explicit time integration

In sheet-material-forming applications, explicit dynamic integration is commonly used because it avoids the repeated global nonlinear solves required by implicit methods and can handle complex tool-blank contact efficiently [3, 5, 40]. Time is discretised as $t^n = n \Delta t$, where Δt is the time increment. Quantities evaluated at t^n are denoted by the superscript n , and half-step velocities are denoted by $n \pm \frac{1}{2}$.

The semi-discrete nodal equilibrium equation at timestep n is written as

$$\mathbf{M} \ddot{\mathbf{u}}^n = \mathbf{P}_{\text{ext}}^n - \mathbf{I}_{\text{int}}^n, \quad (2)$$

where \mathbf{M} is the lumped mass matrix, $\ddot{\mathbf{u}}^n$ is the nodal acceleration vector, $\mathbf{P}_{\text{ext}}^n$ is the external nodal force vector, and $\mathbf{I}_{\text{int}}^n$ is the internal nodal force vector assembled from elemental stress contributions. In forming simulations, $\mathbf{P}_{\text{ext}}^n$ is dominated by tool-blank contact forces, while $\mathbf{I}_{\text{int}}^n$ depends on the current elemental stress state.

Equation (2) gives the acceleration at the current timestep after the external and internal forces have been evaluated. The acceleration is therefore not known a priori for the whole trajectory: it changes with the evolving geometry, contact state, strain, stress, and thickness-related elemental states. The displacement field must consequently be advanced step by step through the explicit time-integration scheme.

2.2. Nodal kinematics and node-to-element strain transfer

2.2.1. Nodal kinematics update

Given the nodal acceleration from Eq. (2), the central-difference scheme updates the half-step velocity as

$$\dot{\mathbf{u}}^{n+\frac{1}{2}} = \dot{\mathbf{u}}^{n-\frac{1}{2}} + \ddot{\mathbf{u}}^n \Delta t, \quad (3)$$

$$\dot{\mathbf{u}}^{1/2} = \dot{\mathbf{u}}^0 + \frac{1}{2} \ddot{\mathbf{u}}^0 \Delta t \quad \text{for the first step.} \quad (4)$$

Here, $\dot{\mathbf{u}}^{n\pm\frac{1}{2}}$ denotes the nodal velocity at the half timesteps. If the blank starts from rest, $\dot{\mathbf{u}}^0 = \mathbf{0}$, so the first-step velocity becomes $\dot{\mathbf{u}}^{1/2} = \frac{1}{2} \ddot{\mathbf{u}}^0 \Delta t$.

The displacement increment over the interval $[t^n, t^{n+1}]$ is then

$$\Delta \mathbf{u}^{n+1} = \dot{\mathbf{u}}^{n+\frac{1}{2}} \Delta t, \quad (5)$$

and the accumulated displacement and current nodal position are updated as

$$\mathbf{u}^{n+1} = \mathbf{u}^n + \Delta \mathbf{u}^{n+1}, \quad (6)$$

$$\mathbf{x}^{n+1} = \mathbf{x}^n + \Delta \mathbf{u}^{n+1}. \quad (7)$$

This convention distinguishes the accumulated displacement \mathbf{u}^{n+1} from the displacement increment $\Delta \mathbf{u}^{n+1}$. In the surrogate formulation introduced later, if the predicted geometry is updated as $\mathbf{x}^{n+1} = \mathbf{x}^n + \Delta \mathbf{u}^{n+1}$ during rollout, then the network output is the displacement increment $\Delta \mathbf{u}^{n+1}$ rather than the accumulated displacement \mathbf{u}^{n+1} .

2.2.2. Node-to-element strain update

After the nodal kinematic update, the displacement information associated with the nodes of each element is transferred to the element integration points. Let $\mathcal{N}(i) = \{v_1, \dots, v_{n_i}\}$ denote the set of nodes connected to element

i. If \mathbf{u}^n denotes the global stacked nodal displacement vector, the element-level nodal displacement vector for element i can be extracted through the connectivity as

$$\mathbf{u}_{\mathcal{N}(i)}^n = \mathbf{S}_i \mathbf{u}^n, \quad \Delta \mathbf{u}_{\mathcal{N}(i)}^{n+1} = \mathbf{S}_i \Delta \mathbf{u}^{n+1}, \quad (8)$$

where \mathbf{S}_i is a Boolean extraction matrix that selects the displacement components of the nodes belonging to element i .

At integration point q of element i , the strain and strain increment are obtained from the element nodal displacement vector through the strain-displacement matrix [3]:

$$\boldsymbol{\varepsilon}_{iq}^n = \mathbf{B}_{iq}^n \mathbf{u}_{\mathcal{N}(i)}^n, \quad (9)$$

$$\Delta \boldsymbol{\varepsilon}_{iq}^{n+1} \approx \mathbf{B}_{iq}^n \Delta \mathbf{u}_{\mathcal{N}(i)}^{n+1}. \quad (10)$$

Here, \mathbf{B}_{iq}^n is the strain-displacement matrix evaluated for element i at integration point q , using the configuration at timestep n . It is constructed from the derivatives of the element shape functions with respect to the current or reference coordinates, depending on the adopted finite-strain formulation. Equation (9) connects the strain at integration point q to the displacements of the nodes in $\mathcal{N}(i)$, while Eq. (10) gives the corresponding incremental strain update over $[t^n, t^{n+1}]$.

This transfer is one of the motivations for the bipartite graph representation introduced in Section 5. In the FE formulation, element-level quantities are not obtained from isolated element features; they are computed from the displacements of the connected nodes through element connectivity and shape-function derivatives.

2.3. Constitutive update and thinning evaluation

With the strain increment obtained at each integration point, the material constitutive update gives the stress increment. In compact linearised notation, this can be written as

$$\Delta \boldsymbol{\sigma}_{iq}^{n+1} = \mathbf{C}_{iq}^n \Delta \boldsymbol{\varepsilon}_{iq}^{n+1}, \quad (11)$$

$$\boldsymbol{\sigma}_{iq}^{n+1} = \boldsymbol{\sigma}_{iq}^n + \Delta \boldsymbol{\sigma}_{iq}^{n+1}, \quad (12)$$

where $\boldsymbol{\sigma}_{iq}^n$ is the stress tensor, and \mathbf{C}_{iq}^n is the material tangent or algorithmic material matrix at integration point q of element i . The precise form of \mathbf{C}_{iq}^n

depends on the constitutive law and may depend on temperature, strain rate, or other internal variables.

In sheet forming, thickness evolution is an important elemental deformation measure. Let th_{iq}^n be the current thickness associated with integration point q of element i , and let th_{iq}^0 be its initial value. Using the through-thickness logarithmic strain convention [5], the accumulated through-thickness strain is

$$\varepsilon_{33,iq}^n = \ln \left(\frac{\text{th}_{iq}^n}{\text{th}_{iq}^0} \right), \quad \text{th}_{iq}^{n+1} = \text{th}_{iq}^n \exp(\Delta\varepsilon_{33,iq}^{n+1}). \quad (13)$$

Here, the subscript 33 denotes the through-thickness direction in the local sheet coordinate system. In a plane-stress sheet formulation, the thickness-direction strain is treated as a dependent quantity. At each explicit timestep, it is recovered during the constitutive update from the in-plane components of the strain increment $\Delta\varepsilon_{iq}^{n+1}$, together with the plastic incompressibility condition [41]. This connection makes thinning an elemental quantity, rather than a purely nodal quantity.

The thinning ratio is defined as

$$\theta_{iq}^n = 1 - \frac{\text{th}_{iq}^n}{\text{th}_{iq}^0} = 1 - \exp(\varepsilon_{33,iq}^n). \quad (14)$$

Here, $\theta_{iq}^n = 0$ indicates no thickness change, $\theta_{iq}^n > 0$ indicates thinning, and $\theta_{iq}^n < 0$ indicates thickening.

2.4. Element-to-node force assembly and contact update

After the stress field is updated at the integration points, the corresponding elemental internal force contributions are mapped back to the connected nodes. For element i , the elemental internal nodal force vector is obtained from the virtual-work relation as

$$\mathbf{f}_{i,\text{int}}^{n+1} = \int_{\Omega_i^{n+1}} (\mathbf{B}_i^{n+1})^\top \boldsymbol{\sigma}_i^{n+1} \, \text{d}\Omega, \quad (15)$$

where Ω_i^{n+1} is the current domain of element i , $\text{d}\Omega$ is the differential measure over that domain, \mathbf{B}_i^{n+1} is the strain-displacement matrix over the element, and $\boldsymbol{\sigma}_i^{n+1}$ is the updated stress field. The transpose of \mathbf{B}_i^{n+1} appears because stresses are mapped to equivalent nodal forces through the virtual-work statement.

In practice, Eq. (15) is evaluated by numerical quadrature. Let $q = 1, \dots, n_q$ index the integration points of element i , where n_q is the number of integration points. The quadrature form is

$$\mathbf{f}_{i,\text{int}}^{n+1} \approx \sum_{q=1}^{n_q} w_q (\mathbf{B}_{iq}^{n+1})^\top \boldsymbol{\sigma}_{iq}^{n+1} J_{iq}^{n+1}. \quad (16)$$

where w_q is the quadrature weight, J_{iq}^{n+1} is the corresponding Jacobian or integration-measure factor, and \mathbf{B}_{iq}^{n+1} and $\boldsymbol{\sigma}_{iq}^{n+1}$ are evaluated at integration point q .

The global internal force vector is then assembled by scattering the elemental contributions into the connected nodal degrees of freedom:

$$\mathbf{I}_{\text{int}}^{n+1} = \sum_{i=1}^{N_e} \mathbf{S}_i^\top \mathbf{f}_{i,\text{int}}^{n+1}. \quad (17)$$

where N_e is the total number of elements. Since \mathbf{S}_i extracts the degrees of freedom associated with element i from the global nodal vector, its transpose \mathbf{S}_i^\top scatters the element-level nodal force vector back into the corresponding entries of the global internal force vector.

In addition to the internal force vector, external nodal forces are evaluated from boundary conditions and tool-blank contact. For each slave node in contact, the contact algorithm evaluates the gap between the blank node and the tool surface, the projected contact point, and the local tool normal. These quantities determine the direction and magnitude of the contact contribution to $\mathbf{P}_{\text{ext}}^{n+1}$ according to the contact formulation used by the FE solver.

The explicit update cycle is then repeated: contact and other external forces are evaluated, internal forces are assembled from the updated elemental stresses, Eq. (2) gives the next nodal acceleration, and Eqs. (3)-(7) update the nodal kinematics. This cycle creates a bidirectional dependency between nodal and elemental quantities. Nodal displacement increments drive elemental strain, stress, and thinning updates through Eqs. (8)-(10), while elemental stresses are assembled back into nodal internal forces through Eqs. (15)-(17).

The proposed model does not explicitly solve the FE equations reviewed in this section, nor does it impose equilibrium or constitutive constraints during training. Instead, these equations are used to identify the nodal-elemental dependency pattern of the FE update. This dependency pattern is then reflected in the graph representation and message-passing architecture introduced in the following sections.

3. Overview of the proposed CAtt-BiGNN model architecture

Based on the FE derivations established in Section 2, we propose the CAtt-BiGNN model, which is inspired by explicit dynamic FE formulations. A general workflow of its hierarchical extension (CAtt-BiUGNN) is presented in Figure 1. CAtt-BiUGNN retains the same bipartite message-passing scheme as CAtt-BiGNN, while introducing a downsampling and up-sampling mechanism to improve scalability on large graphs. The workflow begins with the generation of simulation data (Section 4), from which both nodal and elemental states are extracted. These states are then preprocessed into an FE-inspired bipartite graph representation (Section 5). In this representation, nodes and elements are treated as graph entities, while graph edges encode geometric relations. The subsequent step is the model development (Section 6), which follows an encoder–processor–decoder design with skip connections. In this design, message passing is integrated with a cross-attention mechanism to fuse nodal and elemental information across different scales. Once trained, the model performs autoregressive rollout from the undeformed configuration and dynamically recomputes contact features at each predicted timestep to ensure consistency with the evolving geometry. The model directly outputs both nodal kinematics and elemental states such as thinning fields. This removes the need for interpolation and complex post-processing. The model evaluation is presented in Section 8. It assesses field-level accuracy over time using quantitative error metrics, compares the proposed model with baseline surrogates, and examines robustness during autoregressive rollout across representative forming cases.

4. Dataset generation

The FE simulations were recorded at 11 discrete timesteps, following the standard output settings commonly used in commercial sheet-forming solvers. The first timestep corresponds to the undeformed initial configuration, while the remaining ten timesteps describe the progressive deformation of the blank throughout the forming process. Such temporal resolution is typically sufficient to capture the overall deformation evolution and the key stages relevant for manufacturability evaluation and design analysis.

Two benchmark forming scenarios were considered in this study: a dome-shaped case representing cold forming and a corner-shaped case representing hot forming. The corresponding simulation configurations and dataset generation procedures are presented in the following subsections.

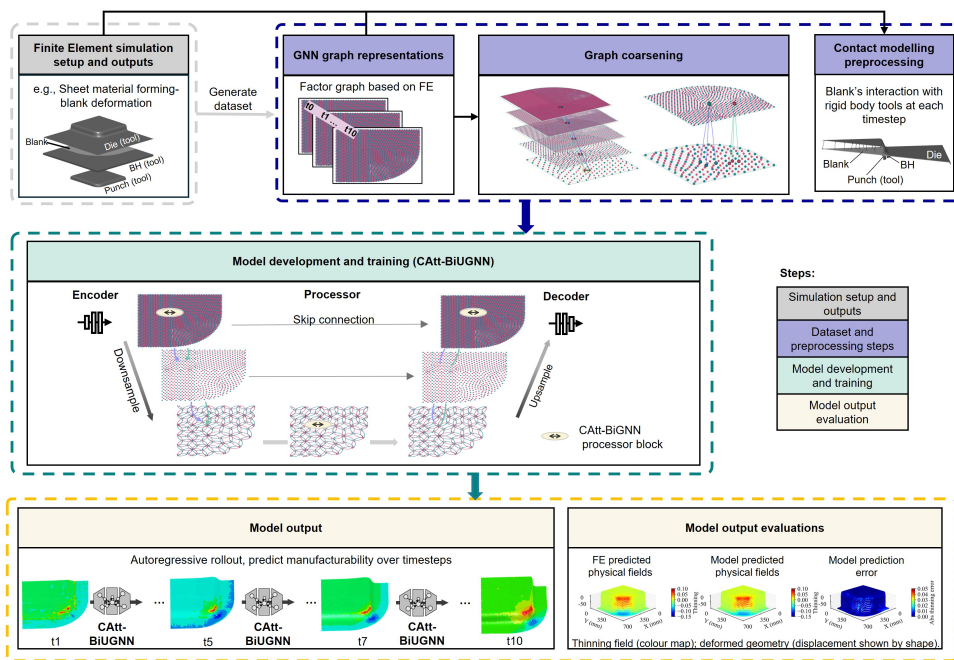


Figure 1: Overview of the proposed CAtt-BiUGNN workflow for autoregressive nodal-elemental field prediction.

4.1. Dome-shaped geometry

The dome-shaped geometry has a double-curvature surface, which leads to a more complex stress and deformation state than single-curvature geometries. For this reason, it is often used as a baseline to evaluate manufacturability [42]. Figure 2 summarises the cold-stamping configuration used in this work. The die, punch, blank holder, and spacers are modelled as rigid bodies, whereas the blank is treated as deformable. The die remains fully constrained. The punch travels vertically at a constant stamping speed of 500 mm/s to draw the blank into the die cavity. To stabilise the flange region and suppress wrinkling, a blank holding force of 200 kN is applied to the blank holder. Spacers of thickness 2.2 mm are inserted between the die and the blank holder to introduce a controlled offset, which promotes more stable material flow. The blank material follows a simplified isotropic constitutive law for cold-work Al2008, taken from the PAM-STAMP material database. The initial blank thickness is 2 mm, and the friction coefficient is set to 0.12.

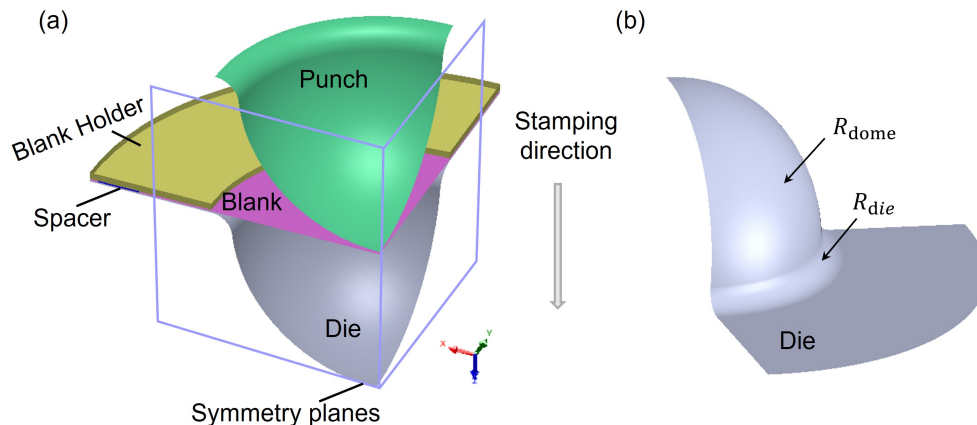


Figure 2: Dome case study (a) simulation setup (b) geometry parameter variables

A family of dome-shaped tool geometries is generated using the geometry parameter variables in Figure 2(b). Two geometric parameters define the die profile: the dome radius R_{dome} and the die radius R_{die} . The DoE ranges are $60 \text{ mm} \leq R_{dome} \leq 120 \text{ mm}$ and $10 \text{ mm} \leq R_{die} \leq 20 \text{ mm}$. The punch geometry is constructed by applying a 2 mm offset with respect to the die. To reduce computational cost, only one quarter of the dome is simulated. Symmetry planes are imposed as boundary conditions, and the same uniform quarter-circle blank is used for all cases.

Dataset generation is fully automated and follows the workflow reported in [8]. Latin Hypercube Sampling (LHS) is used to draw tool-parameter combinations within the prescribed DoE ranges. Training, validation, and test subsets are sampled independently to improve design-space coverage and to reduce the risk of distribution leakage across splits. For each sampled design, tool geometries are created programmatically in SolidWorks, meshed using HyperMesh, and then simulated in PAM-STAMP. The resulting dataset contains 50 training cases, 25 validation cases, and 25 test cases. Each case corresponds to a unique tool configuration and provides stamping outputs over 11 timesteps, which capture the deformation evolution under varying tool geometries.

4.2. Corner-shaped geometry

A hot-formed deep drawn corner case study was considered, as illustrated in Figure 3. The die geometry was defined by four design variables: the die corner radius R_{die} , the punch radius R_{punch} , the plan view radius R_{planview} , and the overall height H . The parameter ranges were specified as $25 \text{ mm} \leq R_{\text{die}} \leq 40 \text{ mm}$, $20 \text{ mm} \leq R_{\text{punch}} \leq 27.3 \text{ mm}$, $70 \text{ mm} \leq R_{\text{planview}} \leq 250 \text{ mm}$, and $60 \text{ mm} \leq H \leq 120 \text{ mm}$. The punch geometry was defined with a constant offset of 2.3 mm with respect to the die. For all simulations, a single blank geometry was used throughout the dataset, with the blank shape kept unchanged across all cases. The sampling of tool configurations followed a Design of Experiment (DoE) strategy. Parameter combinations were generated using Latin Hypercube Sampling (LHS) within the specified bounds. For each sampled configuration, the CAD model of the tool set was generated automatically. The geometries were subsequently meshed in HyperMesh and then analysed in PAM-STAMP through an automated simulation workflow.

An elastic-viscoplastic material model of AA6082 under hot-stamping conditions was adopted for the corner-shaped simulations [8, 43]. The sheet was initially heated to 500 °C, whereas the forming tools were maintained at 25 °C. A stamping velocity of 500 mm/s was applied during forming. The spacer thickness was set to 2.3 mm and the blank thickness was set to 2 mm. To control material flow during forming, a blank holding force of 200 kN was applied through the blank holder in the direction opposite to the stamping motion. In the simulation setup, the punch remained fully constrained while the die translated in the negative z -direction, with the stroke determined by the geometric configuration (total height) of the die.

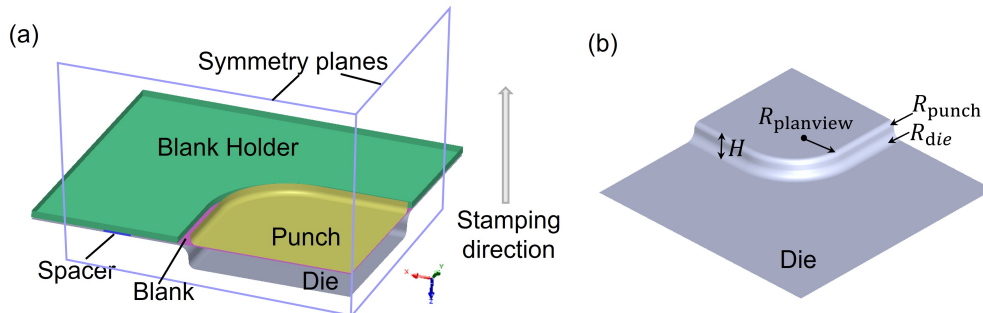


Figure 3: Corner case study (a) simulation setup (b) geometry parameter variables

Based on the defined DoE parameter space and process configuration, batch finite element simulations were performed in PAM-STAMP to construct the dataset. Three independent simulation batches were executed, producing 100 training samples, 25 validation samples, and 25 test samples. Each simulation was recorded at 11 discrete timesteps, yielding a temporal sequence that captures the evolution of sheet deformation under different tool geometries.

5. Bipartite graph representation

Based on the explicit FE formulation introduced in Section 2, we construct a bipartite graph representation that reflects the bidirectional information exchange between nodal and elemental variables. This bipartite graph representation is shown in Figure 4. Starting from the original FE mesh, two types of graph nodes are defined: mesh nodes, which represent nodal degrees of freedom, and element centre-nodes, which represent element-level states obtained from the corresponding elemental or integration-point quantities. Rather than adopting the original mesh edges as graph connections, the graph is built with bidirectional links between each element and its associated mesh nodes. This construction is motivated by the FE coupling described in Section 2: nodal displacement increments are transferred to elements for strain and thickness-related updates, while elemental stress contributions are assembled back to nodes through the internal force vector.

Following the bipartite graph representation, graph input and output features are defined in Table 1. In the following, mesh node refers to a mesh node v , and an element centre-node refers to a finite element i . The notation

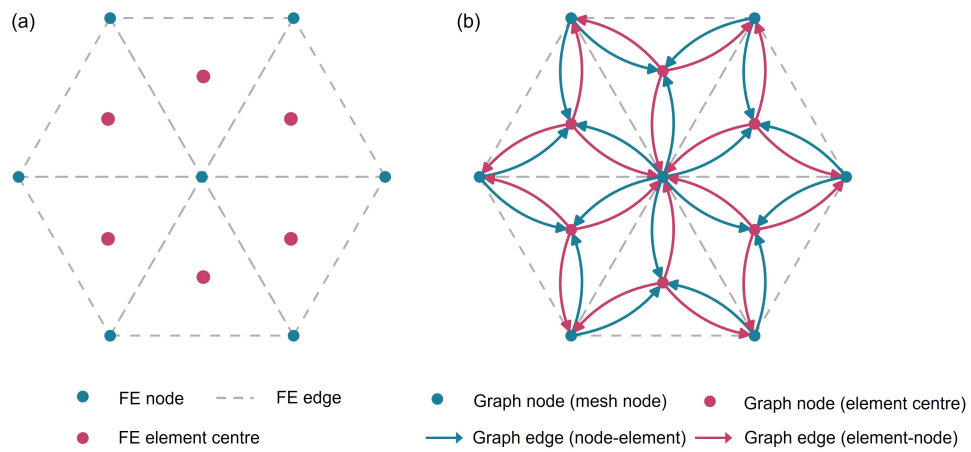


Figure 4: Bipartite graph construction. (a) FE mesh with mesh nodes, FE mesh edges, and elemental quantities located at element centres or representative integration points. (b) Bipartite graph in which mesh-nodes and element centre-nodes are connected by directed node-to-element and element-to-node edges. Dashed FE mesh edges are shown only to indicate the original mesh connectivity and are not used as graph message-passing edges

is chosen to be consistent with Section 2. The nodal position at timestep n is denoted by \mathbf{x}_v^n , the accumulated nodal displacement by \mathbf{u}_v^n , and the one-step displacement increment by $\Delta\mathbf{u}_v^{n+1}$. The element-level thinning value θ_i^n denotes the thinning value stored for element i in the surrogate dataset. It represents the element-level FE output associated with the integration-point thinning response θ_{iq}^n defined in Eq. (14).

The mesh node input feature vector is constructed in a form motivated by the explicit FE formulation. The nodal displacement-increment input $\Delta\mathbf{u}_v^n$ represents the most recent one-step nodal motion available at timestep n , consistent with the explicit kinematic update in Eq. (5). The boundary indicator \mathbf{b}_v represents fixed degrees of freedom in the three coordinate directions. To incorporate tool-blank contact, the contact-related feature \mathbf{c}_v^n includes the signed tool-blank gap distance d_v^n from node v to the rigid tool surface and the local tool surface normal \mathbf{n}_v^n . These quantities correspond to the contact update discussed in Section 2.4. The mesh node output is defined as the predicted displacement increment $\Delta\mathbf{u}_v^{n+1}$, which advances the nodal position through Eq. (7). During autoregressive rollout, the predicted displacement increment is used as the nodal displacement-increment input for the next step, while the updated nodal position \mathbf{x}_v^{n+1} is used to recompute geometry-dependent edge features and contact-related node features. The global input l represents the stroke value that determines the travel distance of the rigid body tools.

Graph edge input features represent the geometric relation between mesh nodes and their associated element centre-nodes. For element centre-node i , the set of connected nodes is denoted by $\mathcal{N}(i)$, consistent with Section 2.2.2. The element centre-node position \mathbf{x}_i^n is taken as the element-centre position at timestep n , and $\Delta\mathbf{x}_{v,i}^n = \mathbf{x}_v^n - \mathbf{x}_i^n$ denotes the mesh node position relative to the element centre. The Euclidean distance $\|\Delta\mathbf{x}_{v,i}^n\|_2$ is rotation-invariant, while the coordinate-difference vector $\Delta\mathbf{x}_{v,i}^n$ retains directional information. The same geometric descriptor is used for both $\mathbf{e}_{v \rightarrow i}^n$ and $\mathbf{e}_{i \rightarrow v}^n$. This is because the descriptor characterises the shared node-element pair geometry rather than a source-to-target direction vector; the two directions of information transfer are distinguished by the corresponding message-passing update. This shared descriptor also allows the two directed edge types to use the same edge-feature initialisation, reducing parameter count and computational cost. The Reference-configuration edge features at t^0 are included together with the current-configuration features at t^n , so the model receives both a fixed geometric baseline and an updated description of the evolving geometry.

Table 1: Input and output features in the bipartite graph representation.

Symbol	Type	Features
$\mathbf{v}_v^n, \mathbf{c}_v^n$	Mesh node input	$\mathbf{v}_v^n = [\Delta \mathbf{u}_v^n, \mathbf{b}_v]$ $\mathbf{b}_v = (b_{v,x}, b_{v,y}, b_{v,z}) \in \{0, 1\}^3$ $\mathbf{c}_v^n = [d_v^n, \mathbf{n}_v^n]$
\mathbf{s}_i^n	Element centre-node input	$\mathbf{s}_i^n = \theta_i^n$
l	Global input	$l = \text{stroke}$
$\mathbf{e}_{v \rightarrow i}^n$	Node-to-element edge input	$\mathbf{e}_{v \rightarrow i}^n = [\ \Delta \mathbf{x}_{v,i}^0\ _2, \Delta \mathbf{x}_{v,i}^0, \ \Delta \mathbf{x}_{v,i}^n\ _2, \Delta \mathbf{x}_{v,i}^n]$ $\ \Delta \mathbf{x}_{v,i}^n\ _2 = \sqrt{(\Delta x_{v,i}^n)^2 + (\Delta y_{v,i}^n)^2 + (\Delta z_{v,i}^n)^2}$
$\mathbf{e}_{i \rightarrow v}^n$	Element-to-node edge input	$\mathbf{e}_{i \rightarrow v}^n = [\ \Delta \mathbf{x}_{v,i}^0\ _2, \Delta \mathbf{x}_{v,i}^0, \ \Delta \mathbf{x}_{v,i}^n\ _2, \Delta \mathbf{x}_{v,i}^n]$
$\mathbf{v}_v^{n,\text{out}}$	Mesh node output	$\mathbf{v}_v^{n,\text{out}} = \Delta \mathbf{u}_v^{n+1}$
$\mathbf{s}_i^{n,\text{out}}$	Element centre-node output	$\mathbf{s}_i^{n,\text{out}} = \theta_i^{n+1}$

This edge design follows the FE-inspired node-element information flow described in Section 2. In the FE formulation, nodal displacement increments are extracted through the element connectivity and transferred to element integration points, as described by Eqs. (8)-(10). Conversely, elemental stress contributions are assembled back into the global internal force vector through Eq. (17). The bipartite graph does not explicitly evaluate these FE operators, but its two directed edge sets provide a learning structure that reflects the same node-to-element and element-to-node exchange. The use of relative geometric features is also consistent with mesh-based GNN practice [19].

In the present sheet-forming application, the element centre-node input feature is defined as the element-level thinning indicator θ_i^n , corresponding to the thinning definition in Eq. (14). The element centre-node output is the predicted thinning value θ_i^{n+1} at the subsequent timestep. In this way, the model learns to predict nodal displacement increments and elemental thinning evolution on their native FE domains. The model can therefore learn coupled nodal kinematics and element-level deformation evolution without relying on node-element interpolation as a post-processing step.

6. CAtt-BiGNN model development

This section introduces the proposed cross-attention-based bipartite graph neural network, denoted as CAtt-BiGNN, and its hierarchical extension, CAtt-BiUGNN. The graph representation introduced in Section 5 contains two types of graph nodes: mesh-nodes, which carry nodal kinematic and contact information, and element centre-nodes, which carry element-level deformation information. The model exchanges information between these two domains through directed node-to-element and element-to-node edges. This design follows the node-to-element and element-to-node transfer pattern discussed in Section 2, while remaining a data-driven surrogate rather than an explicit enforcement of the full finite-element equilibrium equations.

To keep the notation consistent with Sections 2 and 5, the nodal position at timestep n is denoted by \mathbf{x}_v^n , the accumulated nodal displacement by \mathbf{u}_v^n , and the one-step displacement increment by $\Delta\mathbf{u}_v^{n+1}$. Following Table 1, the model mesh node output is denoted by $\mathbf{v}_v^{n,\text{out}}$ and corresponds to $\Delta\mathbf{u}_v^{n+1}$, while the model element centre-node output is denoted by $\mathbf{s}_i^{n,\text{out}}$ and corresponds to θ_i^{n+1} . A hat symbol is reserved for latent neural-network representations, such as $\hat{\mathbf{v}}_{v,L}^n$, rather than for the physical graph input or output variables.

6.1. General description of the CAtt-BiGNN architecture

The CAtt-BiGNN follows an encoder-processor-decoder structure, as illustrated in Figure 5. At timestep n , the graph input contains mesh node features \mathbf{v}_v^n , contact features \mathbf{c}_v^n , element centre-node features \mathbf{s}_i^n , directed node-to-element edge features $\mathbf{e}_{v \rightarrow i}^n$, directed element-to-node edge features $\mathbf{e}_{i \rightarrow v}^n$, and the global stroke input l , as defined in Table 1.

The implementation uses one encoder for mesh node features, three tool-specific encoders for contact features, one encoder for element features, one shared encoder for both directed edge types, and one encoder for the global stroke-related feature. The contact feature \mathbf{c}_v^n in Table 1 is implemented as separate die, punch, and blank-holder contact descriptors. Their encoded latent features are denoted by $\hat{\mathbf{c}}_{v,D}^n$, $\hat{\mathbf{c}}_{v,P}^n$, and $\hat{\mathbf{c}}_{v,BH}^n$, respectively. The encoded latent features before the first processor layer are

$$\begin{aligned} \hat{\mathbf{v}}_{v,0}^n &= f_{\text{en}}^v(\mathbf{v}_v^n), & \hat{\mathbf{s}}_{i,0}^n &= f_{\text{en}}^s(\mathbf{s}_i^n), \\ \hat{\mathbf{c}}_{v,D}^n &= f_{\text{en}}^{c,D}(\mathbf{c}_{v,D}^n), & \hat{\mathbf{c}}_{v,P}^n &= f_{\text{en}}^{c,P}(\mathbf{c}_{v,P}^n), \\ \hat{\mathbf{c}}_{v,BH}^n &= f_{\text{en}}^{c,BH}(\mathbf{c}_{v,BH}^n), & \hat{l} &= f_{\text{en}}^g(l), \\ \hat{\mathbf{e}}_{v \rightarrow i,0}^n &= f_{\text{en}}^e(\mathbf{e}_{v \rightarrow i}^n), & \hat{\mathbf{e}}_{i \rightarrow v,0}^n &= f_{\text{en}}^e(\mathbf{e}_{i \rightarrow v}^n). \end{aligned} \tag{18}$$

Here, f_{en}^v , f_{en}^s , $f_{\text{en}}^{c,D}$, $f_{\text{en}}^{c,P}$, $f_{\text{en}}^{c,BH}$, f_{en}^g , and f_{en}^e denote the encoder networks for the mesh-node feature vector, element centre-node feature vector, die contact feature vector, punch contact feature vector, blank-holder contact feature vector, global stroke input, and directed edge feature vector, respectively. The notation $\hat{(\cdot)}$ denotes an encoded latent representation. The subscript 0 denotes the latent feature before the first processor layer. The same edge encoder f_{en}^e is applied to both $\mathbf{e}_{v \rightarrow i}^n$ and $\mathbf{e}_{i \rightarrow v}^n$, because the two directed edge inputs use the same node-element pair descriptor defined in Table 1. The direction of information transfer is represented by the corresponding processor update.

After the processor and hierarchical update stages, the final latent mesh node and element centre-node states are decoded to the graph outputs defined in Table 1. In the implementation, the mesh node decoder receives the final mesh node latent feature together with the initial encoded mesh node skip feature and the three encoded contact features. The element centre-node decoder receives the final element centre-node latent feature together with

the initial encoded centre-node skip feature. The decoded outputs are

$$\begin{aligned}\mathbf{v}_v^{n,\text{out}} &= \Delta \mathbf{u}_v^{n+1} = f_{\text{de}}^{\text{node}} \left([\hat{\mathbf{v}}_v^{n,\text{final}}; \hat{\mathbf{v}}_{v,0}^n; \hat{\mathbf{c}}_{v,D}^n; \hat{\mathbf{c}}_{v,P}^n; \hat{\mathbf{c}}_{v,BH}^n] \right), \\ \mathbf{s}_i^{n,\text{out}} &= \theta_i^{n+1} = f_{\text{de}}^{\text{elem}} \left([\hat{\mathbf{s}}_i^{n,\text{final}}; \hat{\mathbf{s}}_{i,0}^n] \right).\end{aligned}\tag{19}$$

During autoregressive rollout, the decoded node output $\mathbf{v}_v^{n,\text{out}}$ is accumulated to update the nodal displacement and nodal position:

$$\mathbf{u}_v^{n+1} = \mathbf{u}_v^n + \mathbf{v}_v^{n,\text{out}}, \quad \mathbf{x}_v^{n+1} = \mathbf{x}_v^n + \mathbf{v}_v^{n,\text{out}}.\tag{20}$$

The updated nodal positions and element states are then used to construct the graph input for the next rollout timestep. In particular, geometry-dependent edge features and contact descriptors are recomputed from the updated geometry whenever they depend on the current nodal positions.

The processor is the core of the architecture. Each processor layer performs a closed message-passing cycle between nodes and elements. First, node-to-element edge features are updated and aggregated to update the element states. Second, element-to-node edge features are updated and aggregated to update the nodal states. This sequence mirrors the FE-inspired transfer pattern in which nodal kinematic information is used to update element-level quantities, while element-level information is subsequently propagated back to nodal states. The processor is therefore FE-inspired and domain-aligned, but it does not explicitly enforce stress equilibrium or constitutive consistency. A number of processor layers are applied to extend the message-passing range. A tailored cross-attention mechanism is included to enable weighted node-element coupling, as detailed in Section 6.2. The model can operate on a single high-resolution graph and can also be combined with the downsampling and upsampling mechanism described in Section 6.3. When integrated with this multiscale structure, the model forms the hierarchical variant CAtt-BiUGNN.

6.2. Cross-attention-based processor block

The cross-attention-based processor assigns adaptive weights to directed node-element messages. The purpose of the attention mechanism is to let the receiver state decide which incoming geometric relations are most relevant at the current deformation state. In the node-to-element direction, the receiver is an element centre-node and the incoming messages originate

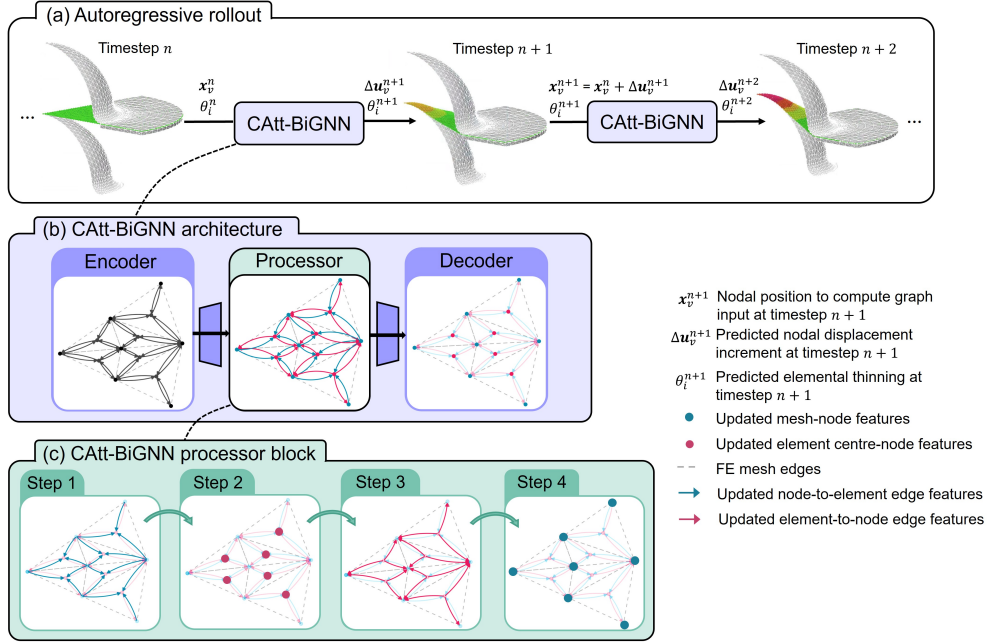


Figure 5: CAtt-BiGNN architecture and autoregressive rollout. At timestep n , the encoded nodal, contact, elemental, and directed edge features are processed by node-element message-passing layers and decoded into the nodal displacement increment and elemental thinning. The nodal position is updated, and geometry-dependent features are recomputed for the next rollout step. Step (1)-(4) show the four processor substeps: node-to-element edge update, element centre-node update, element-to-node edge update, and mesh-node update.

from connected mesh nodes. In the element-to-node direction, the receiver is a mesh-node and the incoming messages originate from connected element centre-nodes.

Consistent with Section 5, let $\mathcal{N}(i)$ denote the set of mesh nodes connected to element centre-node i . The reverse adjacency set for a mesh node v is denoted by $\mathcal{M}(v) = \{i \mid v \in \mathcal{N}(i)\}$. The corresponding directed edge sets can be written as

$$\mathcal{E}_{\text{in}}^{v \rightarrow i}(i) = \{(v, i) \mid v \in \mathcal{N}(i)\}, \quad \mathcal{E}_{\text{in}}^{i \rightarrow v}(v) = \{(i, v) \mid i \in \mathcal{M}(v)\}. \quad (21)$$

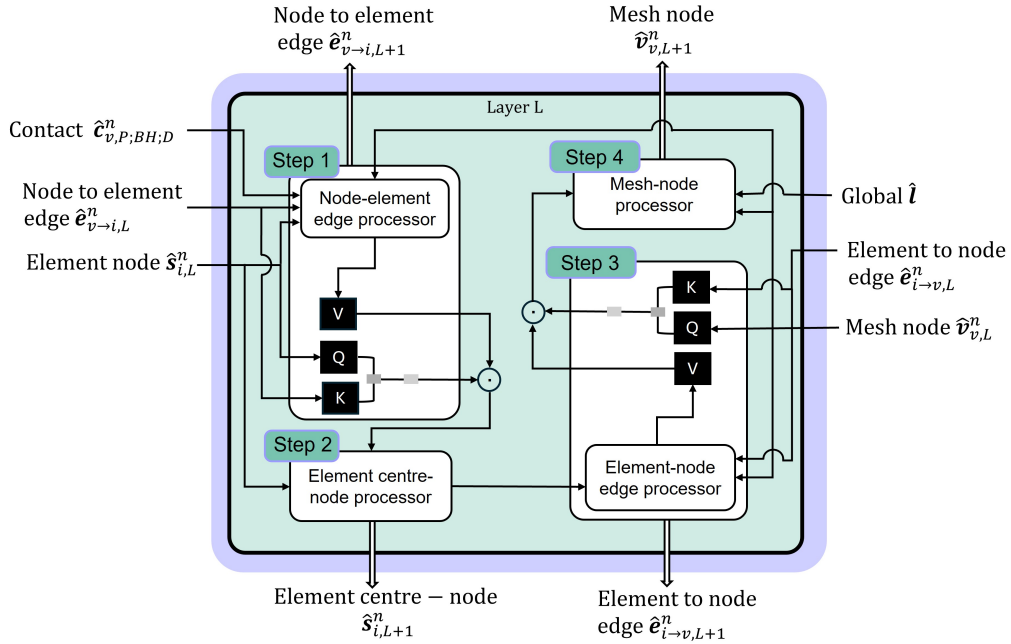


Figure 6: Cross-attention-based CAtt-BiGNN processor block. Each processor layer updates node-to-element edges, element centre-node features, element-to-node edges, and mesh-node features in four residual substeps.

Figure 6 can be read as four steps within one processor layer: (1) update node-to-element edge states, (2) aggregate node-to-element messages and update element centre-node states, (3) update element-to-node edge states, and (4) aggregate element-to-node messages and update mesh node states. In the attention operation, the receiver state forms the query \mathbf{Q} , the directed edge state forms the key \mathbf{K} , and the updated directed edge state forms the

value/message vector \mathbf{V} . This makes the attention weights explicitly edge-aware.

6.2.1. Message passing with attention-modulated aggregation

This subsection describes the data flow within one CAtt-BiGNN processor layer, following the four numbered operations in Figure 6. The message passing layer index is denoted by L , and the timestep index is denoted by n . At the beginning of layer L , $\hat{\mathbf{v}}_{v,L}^n$ denotes the latent feature of mesh node v , $\hat{\mathbf{s}}_{i,L}^n$ denotes the latent feature of element i , $\hat{\mathbf{e}}_{v \rightarrow i,L}^n$ denotes the latent feature of the directed node-to-element edge $v \rightarrow i$, and $\hat{\mathbf{e}}_{i \rightarrow v,L}^n$ denotes the latent feature of the directed element-to-node edge $i \rightarrow v$. The contact latent features of node v are denoted by $\hat{\mathbf{c}}_{v,D}^n$, $\hat{\mathbf{c}}_{v,P}^n$, and $\hat{\mathbf{c}}_{v,BH}^n$, corresponding to the die, punch, and blank-holder contact descriptors.

Step 1: node-to-element edge update. For each directed edge $v \rightarrow i$, the node-to-element edge processor updates the edge latent feature:

$$\hat{\mathbf{e}}_{v \rightarrow i,L+1}^n = \hat{\mathbf{e}}_{v \rightarrow i,L}^n + f_{v \rightarrow i}^e(\hat{\mathbf{v}}_{v,L}^n, \hat{\mathbf{c}}_{v,D}^n, \hat{\mathbf{c}}_{v,P}^n, \hat{\mathbf{c}}_{v,BH}^n, \hat{\mathbf{e}}_{v \rightarrow i,L}^n), \quad (22)$$

where $f_{v \rightarrow i}^e$ is a learnable node-to-element edge-update function. Step 1 produces the updated edge feature $\hat{\mathbf{e}}_{v \rightarrow i,L+1}^n$ and the attention weight $\alpha_{v \rightarrow i,L}^n$. The updated edge feature is used as the node-to-element message,

$$\mathbf{V}_{v \rightarrow i,L}^n = \hat{\mathbf{e}}_{v \rightarrow i,L+1}^n, \quad (23)$$

The corresponding attention weight $\alpha_{v \rightarrow i,L}^n$ is computed from the receiver query and directed-edge key in Section 6.2.2.

Step 2: element centre-node update. Let $\mathcal{N}(i)$ denote the set of mesh nodes connected to element centre-node i . The messages generated in Step 1 are aggregated at element i :

$$\mathbf{m}_{i,L}^{v \rightarrow i,n} = \sum_{v \in \mathcal{N}(i)} \alpha_{v \rightarrow i,L}^n \mathbf{V}_{v \rightarrow i,L}^n. \quad (24)$$

Here, $\mathbf{m}_{i,L}^{v \rightarrow i,n}$ is the aggregated node-to-element message. This message is used to update the element centre-node latent feature:

$$\hat{\mathbf{s}}_{i,L+1}^n = \hat{\mathbf{s}}_{i,L}^n + f_{v \rightarrow i}^s(\hat{\mathbf{s}}_{i,L}^n, \mathbf{m}_{i,L}^{v \rightarrow i,n}), \quad (25)$$

where $f_{v \rightarrow i}^s$ is a learnable element-update function. Step 2 produces the updated element centre-node feature $\hat{\mathbf{s}}_{i,L+1}^n$, which is then used in the element-to-node edge update.

Step 3: element-to-node edge update. For each directed edge $i \rightarrow v$, the element-to-node edge processor updates the edge latent feature using the updated element centre-node feature from Step 2:

$$\hat{\mathbf{e}}_{i \rightarrow v, L+1}^n = \hat{\mathbf{e}}_{i \rightarrow v, L}^n + f_{i \rightarrow v}^e(\hat{\mathbf{s}}_{i, L+1}^n, \hat{\mathbf{v}}_{v, L}^n, \hat{\mathbf{e}}_{i \rightarrow v, L}^n), \quad (26)$$

where $f_{i \rightarrow v}^e$ is a learnable element-to-node edge-update function. Step 3 produces the updated edge feature $\hat{\mathbf{e}}_{i \rightarrow v, L+1}^n$ and the attention weight $\alpha_{i \rightarrow v, L}^n$. The updated edge feature is used as the element-to-node message,

$$\mathbf{V}_{i \rightarrow v, L}^n = \hat{\mathbf{e}}_{i \rightarrow v, L+1}^n, \quad (27)$$

while $\alpha_{i \rightarrow v, L}^n$ controls its contribution to the receiver mesh node. The computation of $\alpha_{i \rightarrow v, L}^n$ is given in Section 6.2.2.

Step 4: mesh-node update. Let $\mathcal{M}(v) = \{i \mid v \in \mathcal{N}(i)\}$ denote the set of elements connected to mesh node v . The messages generated in Step 3 are aggregated at mesh node v :

$$\mathbf{m}_{v, L}^{i \rightarrow v, n} = \sum_{i \in \mathcal{M}(v)} \alpha_{i \rightarrow v, L}^n \mathbf{V}_{i \rightarrow v, L}^n. \quad (28)$$

Here, $\mathbf{m}_{v, L}^{i \rightarrow v, n}$ is the aggregated element-to-node message. This message, together with the encoded global stroke input \hat{l} , is used to update the mesh-node latent feature:

$$\hat{\mathbf{v}}_{v, L+1}^n = \hat{\mathbf{v}}_{v, L}^n + f_{i \rightarrow v}^v(\hat{\mathbf{v}}_{v, L}^n, \mathbf{m}_{v, L}^{i \rightarrow v, n}, \hat{l}), \quad (29)$$

where $f_{i \rightarrow v}^v$ is a learnable mesh-node update function. Step 4 produces the updated mesh-node feature $\hat{\mathbf{v}}_{v, L+1}^n$, completing one bidirectional node-element message-passing layer.

6.2.2. Attention weight computation in CAtt-BiGNN

Section 6.2.1 introduced the attention weights $\alpha_{v \rightarrow i, L}^n$ and $\alpha_{i \rightarrow v, L}^n$, which are generated by the directed edge processors and then used in the element and mesh-node updates. This subsection describes how these weights are computed. The main design choice in CAtt-BiGNN is that the query is constructed from the receiver state, while the key is constructed from the directed edge state. This is because the receiver node or element determines

what information is required, whereas the edge feature carries the local node-element geometric relation. The updated directed edge feature is then used as the value/message vector in the aggregation step.

For clarity, the node-to-element direction is described first. The element-to-node direction follows the same principle with the receiver changed from an element to a mesh node.

Query and key. For a directed edge from mesh node v to element i , the receiver is element i . The query vector is therefore computed from the element latent feature $\hat{\mathbf{s}}_{i,L}^n$:

$$\mathbf{Q}_{i,L}^n = f_q^s(\hat{\mathbf{s}}_{i,L}^n), \quad \mathbf{K}_{v \rightarrow i,L}^n = f_k^s(\hat{\mathbf{e}}_{v \rightarrow i,L}^n). \quad (30)$$

Here, $\mathbf{Q}_{i,L}^n$ is the query vector of element i , and $\mathbf{K}_{v \rightarrow i,L}^n$ is the key vector of the incoming directed edge $v \rightarrow i$. The functions f_q^s and f_k^s are learnable projection functions that map the element latent feature and the directed edge latent feature into the query and key spaces, respectively.

The value/message vector is the updated node-to-element edge feature produced by Step 1 in Section 6.2.1:

$$\mathbf{V}_{v \rightarrow i,L}^n = \hat{\mathbf{e}}_{v \rightarrow i,L+1}^n. \quad (31)$$

No additional value-projection layer is used; the learned edge update itself provides the message to be weighted and aggregated.

Scaled dot-product score. The unnormalised compatibility score for edge $v \rightarrow i$ is computed by a scaled dot product:

$$\rho_{v \rightarrow i,L}^n = \frac{(\mathbf{Q}_{i,L}^n)^\top \mathbf{K}_{v \rightarrow i,L}^n}{\sqrt{d_h}}, \quad (32)$$

where $\rho_{v \rightarrow i,L}^n$ is the unnormalised attention score, and d_h is the hidden dimension of the query and key vectors.

Softmax over incoming edges. For each receiver element centre-node i , the softmax is evaluated over all incoming node-to-element edges from the connected mesh node set $\mathcal{N}(i)$:

$$\alpha_{v \rightarrow i,L}^n = \frac{\exp(\rho_{v \rightarrow i,L}^n)}{\sum_{v' \in \mathcal{N}(i)} \exp(\rho_{v' \rightarrow i,L}^n)}. \quad (33)$$

Here, $\alpha_{v \rightarrow i, L}^n$ is the normalised attention weight assigned to the directed edge $v \rightarrow i$. Because the weights are softmax-normalised over the incoming edges of the same receiver element centre-node, they satisfy

$$\sum_{v \in \mathcal{N}(i)} \alpha_{v \rightarrow i, L}^n = 1. \quad (34)$$

These weights are then used in Eq. (24) to aggregate the updated node-to-element edge messages.

Element-to-node attention. The element-to-node direction is computed analogously. For a directed edge $i \rightarrow v$, the receiver is mesh node v , so the query is computed from $\hat{\mathbf{v}}_{v, L}^n$, while the key is computed from the directed edge feature $\hat{\mathbf{e}}_{i \rightarrow v, L}^n$:

$$\mathbf{Q}_{v, L}^n = f_q^v(\hat{\mathbf{v}}_{v, L}^n), \quad \mathbf{K}_{i \rightarrow v, L}^n = f_k^v(\hat{\mathbf{e}}_{i \rightarrow v, L}^n), \quad \mathbf{V}_{i \rightarrow v, L}^n = \hat{\mathbf{e}}_{i \rightarrow v, L+1}^n. \quad (35)$$

Here, $\mathbf{Q}_{v, L}^n$ is the query vector of mesh node v , and $\mathbf{K}_{i \rightarrow v, L}^n$ is the key vector of the incoming directed edge $i \rightarrow v$. The functions f_q^v and f_k^v are learnable projection functions that map the mesh node latent feature and the directed edge latent feature into the query and key spaces, respectively. The corresponding unnormalised score and normalised attention weight are

$$\rho_{i \rightarrow v, L}^n = \frac{(\mathbf{Q}_{v, L}^n)^\top \mathbf{K}_{i \rightarrow v, L}^n}{\sqrt{d_h}}, \quad (36)$$

$$\alpha_{i \rightarrow v, L}^n = \frac{\exp(\rho_{i \rightarrow v, L}^n)}{\sum_{i' \in \mathcal{M}(v)} \exp(\rho_{i' \rightarrow v, L}^n)}. \quad (37)$$

Here, $\rho_{i \rightarrow v, L}^n$ is the unnormalised attention score, $\mathcal{M}(v) = \{i \mid v \in \mathcal{N}(i)\}$ is the set of element centre-nodes connected to mesh node v . The resulting weights $\alpha_{i \rightarrow v, L}^n$ are used in Eq. (28) to aggregate the updated element-to-node edge messages.

Overall, this attention design makes the node-element coupling edge-aware. The receiver state determines the query, the directed edge state determines the key, and the updated directed edge feature provides the message being weighted. This allows the processor to adapt the strength of node-element information exchange according to the local geometric relation encoded on each edge.

6.3. Downsampling and upsampling mechanism

For large sheet-forming graphs, applying many CAtt-BiGNN processor layers directly on the finest graph can be computationally expensive and may limit the effective receptive field. To address this, the proposed model is extended to a hierarchical architecture, denoted as CAtt-BiUGNN. As shown in Figure 7, the model first applies CAtt-BiGNN processor layers on the original fine graph, then transfers the mesh node and element centre-node latent features to coarser graph levels, applies additional CAtt-BiGNN processor layers at the coarsest level, and finally upsamples the features back to the fine graph before decoding.

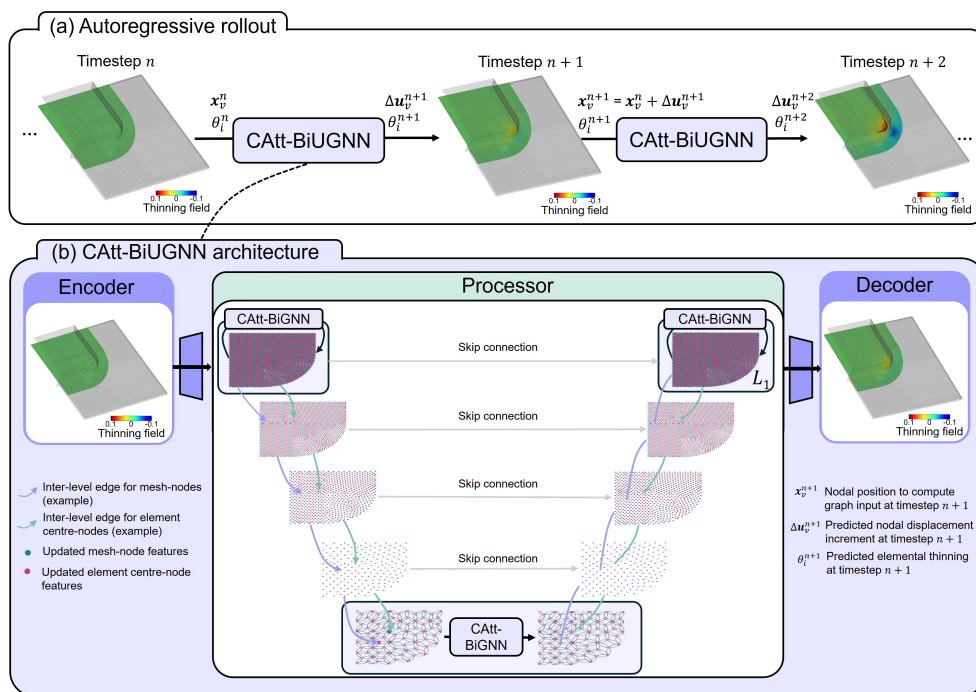


Figure 7: Hierarchical CAtt-BiUGNN architecture. The original fine bipartite graph is encoded and progressively downsampled to lower-resolution graph levels. CAtt-BiGNN processor blocks operate within the hierarchy, while skip connections preserve intermediate latent features. Upsampling transfers the updated lower-resolution-level information back to the fine graph before decoding the nodal displacement increments and elemental thinning values.

The graph hierarchy is indexed by $\ell = 0, 1, \dots, L_g$, where $\ell = 0$ denotes the original high-resolution graph and $\ell = L_g$ denotes the lowest-resolution

graph. The timestep index is denoted by n . Superscript V denotes quantities associated with mesh nodes, and superscript S denotes quantities associated with element centre-nodes. The symbols \downarrow and \uparrow denote downsampling and upsampling operations, respectively. Mesh nodes are indexed by v on level ℓ and by u on level $\ell + 1$. Element centre-nodes are indexed by i on level ℓ and by j on level $\ell + 1$.

Coarsening is applied separately to mesh nodes and element centre-nodes. At each selected graph level, the corresponding mesh node and element centre-node sets form a bipartite graph, so the CAtt-BiGNN processor can be applied. In the corner-shaped case study, four coarsening operations are used, producing five graph levels including the original high-resolution graph, as illustrated in Figure 8.

Inter-level edges define how information is transferred between adjacent graph levels. A k-nearest-neighbour search is used to construct sparse inter-level mappings. The number of nearest neighbours used in the hierarchy is denoted by K_{nn} . In the implementation, each higher-resolution-level node is connected to its K_{nn} nearest lower-resolution-level nodes.

For downsampling from level ℓ to level $\ell + 1$, let $\mathcal{E}_{\downarrow,\ell}^V$ denote the set of inter-level mesh node edges from higher-resolution mesh nodes to lower-resolution mesh nodes, and let $\mathcal{E}_{\downarrow,\ell}^S$ denote the set of inter-level edges from higher-resolution element centre-nodes to lower-resolution element centre-nodes. For a lower-resolution mesh node u and a lower-resolution element centre-node j , the incoming higher-resolution-level neighbour sets are

$$\mathcal{N}_{\downarrow}^V(u) = \{v \mid (v, u) \in \mathcal{E}_{\downarrow,\ell}^V\}, \quad (38)$$

$$\mathcal{N}_{\downarrow}^S(j) = \{i \mid (i, j) \in \mathcal{E}_{\downarrow,\ell}^S\}. \quad (39)$$

Here, $\mathcal{N}_{\downarrow}^V(u)$ is the set of higher-resolution-level mesh nodes connected to lower-resolution mesh node u , and $\mathcal{N}_{\downarrow}^S(j)$ is the set of higher-resolution-level element centre-nodes connected to lower-resolution element centre-node j .

The downsampling operation is applied separately to mesh node and element centre-node latent features. Let $\hat{\mathbf{v}}_{v,\ell}^n$ denote the latent feature of higher-resolution-level mesh node v , and let $\hat{\mathbf{v}}_{u,\ell+1}^n$ denote the resulting latent feature of lower-resolution mesh node u . Similarly, let $\hat{\mathbf{s}}_{i,\ell}^n$ denote the latent feature of higher-resolution-level element centre-node i , and let $\hat{\mathbf{s}}_{j,\ell+1}^n$ denote the resulting latent feature of lower-resolution element centre-node j . The two

downsampling operations are

$$\hat{\mathbf{v}}_{u,\ell+1}^n = \phi \left(\mathbf{a}_{\downarrow,\ell}^V + \sum_{v \in \mathcal{N}_{\downarrow}^V(u)} \mathbf{W}_{v \rightarrow u,\ell}^{\downarrow,V} \hat{\mathbf{v}}_{v,\ell}^n \right), \quad (40)$$

$$\hat{\mathbf{s}}_{j,\ell+1}^n = \phi \left(\mathbf{a}_{\downarrow,\ell}^S + \sum_{i \in \mathcal{N}_{\downarrow}^S(j)} \mathbf{W}_{i \rightarrow j,\ell}^{\downarrow,S} \hat{\mathbf{s}}_{i,\ell}^n \right). \quad (41)$$

Here, $\mathbf{W}_{v \rightarrow u,\ell}^{\downarrow,V}$ is the learnable edge-specific weight matrix for the mesh node inter-level edge (v, u) , and $\mathbf{W}_{i \rightarrow j,\ell}^{\downarrow,S}$ is the corresponding edge-specific weight matrix for the element inter-level edge (i, j) . The vectors $\mathbf{a}_{\downarrow,\ell}^V$ and $\mathbf{a}_{\downarrow,\ell}^S$ are learnable bias vectors for mesh node and element centre-node downsampling, respectively. The activation function is denoted by $\phi(\cdot)$.

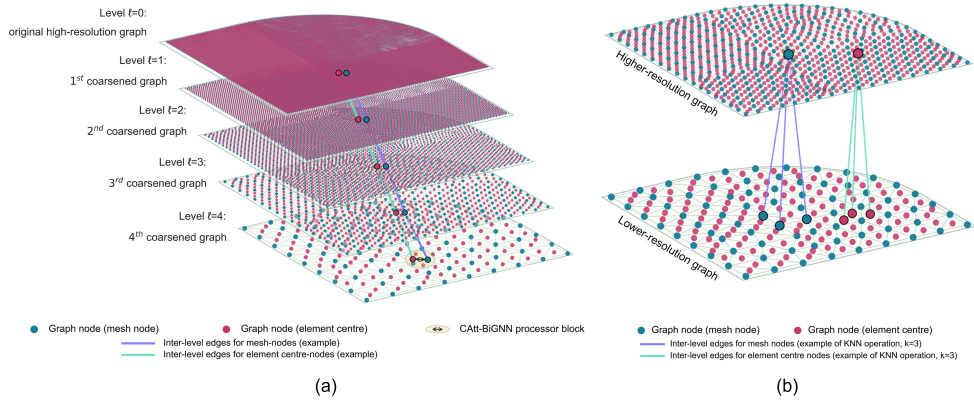


Figure 8: Bipartite graph coarsening and inter-level mapping used in the downsampling and upsampling mechanism. (a) A hierarchy of bipartite graphs is constructed from the original high-resolution graph at level $(\ell = 0)$ to the fourth coarsened graph at level $(\ell = 4)$. Mesh nodes and element centres are represented as two types of graph entities at each level. Example inter-level edges show how mesh node and element-centre features are transferred between adjacent graph levels. (b) Illustration of the (k) -nearest-neighbour inter-level mapping between a higher-resolution graph and a lower-resolution graph, with $(k=3)$ shown as an example. Separate mappings are constructed for mesh nodes and element centres. These mappings are used for downsampling and upsampling in the hierarchical CAtt-BiUGNN architecture.

Upsampling transfers the updated lower-resolution-level features back to higher-resolution level graphs. The upsampling edge sets are the reverse

of the corresponding downsampling mappings. For upsampling from level $\ell + 1$ back to level ℓ , let $\mathcal{E}_{\uparrow,\ell}^V$ denote the set of inter-level edges from lower-resolution mesh nodes to higher-resolution mesh nodes, and let $\mathcal{E}_{\uparrow,\ell}^S$ denote the set of inter-level edges from lower-resolution element centre-node to higher-resolution element centre-node. For a higher-resolution mesh node v and a higher-resolution element centre-node i , the connected lower-resolution-level neighbour sets are

$$\mathcal{N}_{\uparrow}^V(v) = \{u \mid (u, v) \in \mathcal{E}_{\uparrow,\ell}^V\}, \quad (42)$$

$$\mathcal{N}_{\uparrow}^S(i) = \{j \mid (j, i) \in \mathcal{E}_{\uparrow,\ell}^S\}. \quad (43)$$

Here, $\mathcal{N}_{\uparrow}^V(v)$ is the set of lower-resolution mesh nodes connected to higher-resolution mesh node v , and $\mathcal{N}_{\uparrow}^S(i)$ is the set of lower-resolution element centre-node connected to higher-resolution element centre-node i .

Skip connections are used during upsampling to preserve features from the corresponding downsampling stage. Let $\hat{\mathbf{v}}_{u,\ell+1}^{n,\text{up}}$ denote the updated lower-resolution mesh node feature propagated from the coarser part of the network, and let $\hat{\mathbf{v}}_{u,\ell+1}^{n,\text{skip}}$ denote the stored lower-resolution mesh node feature from the corresponding downsampling stage. Similarly, let $\hat{\mathbf{s}}_{j,\ell+1}^{n,\text{up}}$ and $\hat{\mathbf{s}}_{j,\ell+1}^{n,\text{skip}}$ denote the updated and stored lower-resolution element centre-node features. The two upsampling operations are

$$\hat{\mathbf{v}}_{v,\ell}^{n,\text{up}} = \phi \left(\mathbf{a}_{\uparrow,\ell}^V + \sum_{u \in \mathcal{N}_{\uparrow}^V(v)} \mathbf{W}_{u \rightarrow v,\ell}^{\uparrow,V} \left[\hat{\mathbf{v}}_{u,\ell+1}^{n,\text{up}} ; \hat{\mathbf{v}}_{u,\ell+1}^{n,\text{skip}} \right] \right), \quad (44)$$

$$\hat{\mathbf{s}}_{i,\ell}^{n,\text{up}} = \phi \left(\mathbf{a}_{\uparrow,\ell}^S + \sum_{j \in \mathcal{N}_{\uparrow}^S(i)} \mathbf{W}_{j \rightarrow i,\ell}^{\uparrow,S} \left[\hat{\mathbf{s}}_{j,\ell+1}^{n,\text{up}} ; \hat{\mathbf{s}}_{j,\ell+1}^{n,\text{skip}} \right] \right). \quad (45)$$

Here, $[\cdot; \cdot]$ denotes feature concatenation. The matrices $\mathbf{W}_{u \rightarrow v,\ell}^{\uparrow,V}$ and $\mathbf{W}_{j \rightarrow i,\ell}^{\uparrow,S}$ are learnable edge-specific weight matrices for mesh node and element centre-node upsampling, respectively. The vectors $\mathbf{a}_{\uparrow,\ell}^V$ and $\mathbf{a}_{\uparrow,\ell}^S$ are the corresponding bias vectors.

After the final upsampling operation returns information to the original higher-resolution graph, the resulting higher-resolution-level mesh node and element latent features are passed to the decoder described in Section 6.1. The hierarchical architecture therefore combines local node-element coupling on the higher-resolution graph with longer-range information propagation through lower-resolution graph levels.

7. Model training

7.1. Training setup

The models were trained on different computing platforms depending on the case study. For the dome-shaped case study, which contains fewer mesh nodes and elements, training was performed on a workstation equipped with an NVIDIA Quadro 5000 GPU with 16 GB of GPU memory. For the corner-shaped case study, training was conducted on Google Colab using an L4 GPU with 22.5 GB of GPU memory. The dome-shaped case study was trained for 1000 epochs, while the corner-shaped case study was trained for 500 epochs.

All models were trained using the Adam optimiser. The learning rate followed an exponential decay schedule from 10^{-4} to 10^{-6} , consistent with the baseline architectures [19, 26]. Standardisation was applied to the input and output fields before training to improve numerical conditioning and stabilise convergence. The hidden feature dimension was set according to the corresponding model configuration. For the dome-shaped case study, no downsampling or upsampling was used in the architecture, giving a direct comparison between CAtt-BiGNN and conventional mesh-based node-centred GNN baselines. The dome model used 20 message-passing layers. For the larger corner-shaped case study, hierarchical graph downsampling and upsampling were incorporated, as described in Section 6.3, to enable information propagation over longer spatial distances. Following the baseline configuration [26], the hierarchical model used 2 message-passing layers at the highest-resolution graph scale and 10 message-passing layers at the coarsest scale.

The training strategy used teacher forcing. At each prediction transition from t^n to t^{n+1} , the ground-truth graph state at t^n was used as the model input, and the model was trained to predict the next-step nodal displacement increments and elemental thinning value, consistent with the graph-output convention defined in Table 1 and the decoder formulation in Section 6.1. During autoregressive validation and testing, the predicted displacement increment was accumulated to update the nodal position, and the updated geometry was then used to recompute geometry-dependent edge features and contact-related node features for the next timestep.

The total training loss combines the nodal displacement increment loss and the elemental thinning loss. Let M denote the number of trajectories, N_p the number of prediction transitions per trajectory, V the number of mesh nodes, and N_e the number of element centre-nodes. If 11 states are recorded

for one rollout, then $N_p = 10$ prediction transitions. A superscript star denotes the FE reference value, while quantities without a star denote model predictions. In the implementation, the losses are evaluated in the standardised output space; the symbol $\widetilde{(\cdot)}$ denotes the corresponding standardised quantity.

The displacement increment loss is

$$\mathcal{L}_{\text{disp}} = \frac{1}{3MN_pV} \sum_{m=1}^M \sum_{n=0}^{N_p-1} \sum_{v=1}^V \sum_{d \in \{x,y,z\}} \left(\widetilde{\Delta u_{v,d}^{m,n+1}} - \widetilde{\Delta u_{v,d}^{*m,n+1}} \right)^2. \quad (46)$$

Here, $\Delta u_{v,d}^{m,n+1}$ is the predicted displacement increment of mesh node v in Cartesian direction d for trajectory m , and $\Delta u_{v,d}^{*m,n+1}$ is the corresponding FE reference increment. This definition follows the rollout update in which the predicted increment, rather than the accumulated displacement, advances the nodal position.

The thinning loss is

$$\mathcal{L}_{\text{thin}} = \frac{1}{MN_pN_e} \sum_{m=1}^M \sum_{n=0}^{N_p-1} \sum_{i=1}^{N_e} \left(\widetilde{\theta}_i^{m,n+1} - \widetilde{\theta}_i^{*m,n+1} \right)^2, \quad (47)$$

where $\theta_i^{m,n+1}$ and $\theta_i^{*m,n+1}$ are the predicted and FE reference elemental thinning values for element centre-node i , respectively. The total loss is the unweighted sum of the two terms:

$$\mathcal{L}_{\text{total}} = \mathcal{L}_{\text{disp}} + \mathcal{L}_{\text{thin}}. \quad (48)$$

For evaluation and visualisation, the predicted outputs were transformed back from the standardised space to their original physical units before computing the reported physical error metrics.

7.2. Noise injection

When enabled, adaptive Gaussian noise is used as an optional training robustness strategy for autoregressive rollout, rather than as a change to the CAtt-BiGNN or CAtt-BiUGNN architecture itself. The primary architecture-comparison experiments are therefore conducted without noise injection. This setting allows the predictive capacity of different graph architectures to be compared without introducing model-specific noise perturbation tuning. The effect of noise injection is analysed separately using CAtt-BiUGNN as the reference architecture.

The purpose of noise injection is to reduce the train-test mismatch between teacher-forced training and autoregressive rollout. In teacher forcing, the model receives the ground-truth graph state at timestep n . In autoregressive rollout, the graph state at the next timestep is constructed from previously predicted outputs. Small errors in the predicted displacement increment $\Delta \mathbf{u}_v^{n+1}$ can therefore accumulate through the nodal position update and affect the recomputed edge and contact descriptors at later timesteps. In this work, the perturbation is introduced only during teacher-forced training and is applied to the nodal displacement-increment input. Its direct role is to improve the robustness of the kinematic rollout, while any influence on elemental thinning prediction occurs indirectly through the learned node-element coupling.

A commonly used approach is to add zero-mean Gaussian noise with the same scale to all nodal displacement-increment inputs. However, sheet-forming deformation is spatially nonuniform. In forming simulations, nodes in freely deforming areas undergo large displacements, whereas nodes near contact regions may move only slightly but play a dominant role in determining contact forces. The contact features used in our model include inverse-distance terms, which are sensitive when nodes are close to tooling surfaces. Small geometric fluctuations around these near-contact regions can significantly change the contact evaluation. Such errors are amplified during autoregressive rollout because contact descriptors are recomputed from the previously predicted geometry. As a result, uniform Gaussian noise does not adequately reflect this effect in sheet material forming.

To account for this behaviour, the adaptive strategy perturbs the nodal displacement increment $\Delta \mathbf{u}_v^n$ inside the mesh node input feature. The perturbation magnitude is scaled by the inverse displacement-increment magnitude of each mesh node. For mesh node v , the inverse-displacement-increment weight is first computed as

$$\gamma_v^n = \frac{1}{\|\Delta \mathbf{u}_v^n\|_2 + \epsilon}, \quad (49)$$

where ϵ is a small positive constant used to avoid division by zero. The weights are then normalised over the mesh node set \mathcal{V} :

$$\bar{\gamma}_v^n = \frac{\gamma_v^n}{\max_{v' \in \mathcal{V}} \gamma_{v'}^n}. \quad (50)$$

Here, $\bar{\gamma}_v^n \in [0, 1]$ is the adaptive node-wise noise weight. Mesh nodes with smaller displacement-increment magnitudes receive larger weights, while mesh nodes with larger displacement-increment magnitudes receive smaller weights. This gives larger perturbations to slowly moving and contact-sensitive regions, while avoiding excessive perturbation in regions that already undergo large deformation.

The noisy displacement increment used in the mesh node input is then

$$\Delta \mathbf{u}_{v,\text{noise}}^n = \Delta \mathbf{u}_v^n + \bar{\gamma}_v^n \lambda_{\text{noise}} s_{\Delta u}^n \boldsymbol{\eta}_v^n, \quad \boldsymbol{\eta}_v^n \sim \mathcal{N}(\mathbf{0}, \mathbf{I}_3), \quad (51)$$

where $s_{\Delta u}^n$ is the scalar standard deviation of the nodal displacement-increment field, λ_{noise} is a manually tuned global noise-scale factor, and \mathbf{I}_3 is the 3×3 identity matrix. The scale factor λ_{noise} controls the overall strength of the injected perturbation and is selected through validation experiments, rather than being learned by the model. The test set is not used to choose λ_{noise} or any other noise parameter.

During training, only the nodal displacement-increment component of the mesh node input is perturbed. The remaining mesh node, element, edge, contact, and global features are kept unchanged for the same teacher-forced sample, and the training targets remain the original FE-computed displacement increment and elemental thinning value at the next timestep.

During autoregressive rollout, no artificial noise is added. The predicted displacement increment is accumulated to update the nodal position, and the contact-related mesh node features and geometry-dependent edge features are recomputed from the updated predicted geometry, as described in Sections 5 and 6.1.

8. Model performance evaluation

The evaluation is organised to test the modelling choices introduced in the previous sections. The dome-shaped case study uses a smaller graph and is used to isolate the effects of the bipartite node-element representation and the edge-aware attention mechanism without hierarchical downsampling and upsampling. The corner-shaped case study is used to evaluate whether the hierarchical CAtt-BiUGNN architecture can preserve the benefits of edge-aware nodal–elemental coupling on a larger graph under more complex hot-forming conditions.

8.1. Dome-shaped case study

Baseline models. The dome-shaped case study involves relatively small graphs. Therefore, no downsampling or upsampling mechanism is used, allowing the comparison to focus on the bipartite representation and attention mechanism. Six model configurations are evaluated, including: (a) MeshGraphNet (MGN), a widely used GNN-based surrogate model for physical simulations, which performs message passing directly on the original mesh [19]. (b) Recurrent GNN (RGNN), MGN with recurrent updates to better capture temporal dependencies [28]. (c) Vanilla-BiGNN, our BiGNN variant that includes bipartite graph construction but does not apply any attention-based aggregation functions. (d) GAT-BiGNN, BiGNN with GAT-based attention aggregation. (e) CA-BiGNN, BiGNN with pure cross-attention-based aggregation. (f) Our proposed CAtt-BiGNN model, which incorporates the designed edge-based cross-attention aggregation described in Section 6.2. Specifically, the main difference between CA-BiGNN and our proposed CAtt-BiGNN is that CA-BiGNN uses the source mesh node or element centre-node features to compute the Key matrix, whereas our CAtt-BiGNN model uses edge features to compute the Key matrix.

Among all of the comparative models, MGN and RGNN are treated as external baselines, whereas Vanilla-BiGNN, GAT-BiGNN, and CA-BiGNN are treated as ablation models. All models use the recommended hyperparameters from the baseline configurations [19, 28] and the same GPU setup described in Section 7.1. Table 2 summarises the comparison results.

Evaluation metrics. The evaluation metrics are designed to assess the autoregressive prediction accuracy of both nodal geometry evolution and element-level thinning response. Each test trajectory is rolled out autoregressively for ten prediction transitions. The main quantitative metrics are evaluated at the final rollout timestep because the final formed geometry and thinning distribution are the primary quantities used for manufacturability assessment.

Two displacement metrics are used to evaluate final geometry prediction. The mean positional Euclidean error measures the average Euclidean distance between the predicted and FE reference nodal positions at the final rollout timestep. The position mean absolute error (MAE) measures the average absolute coordinate-wise difference between the predicted and FE reference final nodal positions over all mesh nodes and three Cartesian directions. These two metrics evaluate the accuracy of the predicted deformed geometry from complementary vector-distance and coordinate-wise perspectives.

Two thinning-related metrics are used to evaluate element-level thinning prediction at the final rollout timestep. The threshold-based thinning error is computed over the subset of element centre-nodes whose FE reference thinning magnitude exceeds a prescribed threshold. In this work, the threshold is set to 0.005. This setting focuses the evaluation on regions with a meaningful thinning response and reduces the influence of near-zero deformation regions.

The top- $p\%$ critical relative thinning error further evaluates the prediction accuracy in the most thinning-critical region. For each test case, elements are ranked according to their FE reference thinning magnitude at the final rollout timestep, and the top $p\%$ elements are selected as the critical set. The relative thinning error is then averaged over this set. The dome-shaped case uses $p = 5$ because the high-thinning response is more smoothly distributed over the geometry. The corner-shaped case uses $p = 1$ because the critical thinning response is more localised around the sharp geometric transition. These case-specific settings allow the metric to focus on the critical thinning region in each case study.

Results. Table 2 summarises the dome-case ablation results at the final rollout timestep. All relative changes are computed with respect to MGN. Vanilla-BiGNN improves the thinning-related metrics relative to MGN. However, Vanilla-BiGNN does not improve the displacement metrics relative to MGN. This may result from the added coupling between the elemental thinning field and the nodal displacement field. The coupling was expected to facilitate joint learning between the nodal and elemental states; however, the model does not fully capture this dependency effectively. Consequently, inaccuracies in the thinning prediction propagate through the coupling and adversely affect the displacement updates.

Compared with MGN, the proposed CAtt-BiGNN reduces the mean positional Euclidean error by 21.7%, the position MAE by 20.4%, the thresholded thinning error by 35.1%, and the top-5% relative thinning error by 39.9%. GAT-BiGNN does not consistently improve over Vanilla-BiGNN. CA-BiGNN improves over Vanilla-BiGNN, indicating that cross-attention can help modulate node-element message passing. The proposed CAtt-BiGNN gives the best overall balance. In CAtt-BiGNN, the Key matrix is computed from edge features rather than from source mesh node or element centre-node features. This design makes the attention weights directly conditioned on local node–element relations encoded by the directed edges. As a result, the

Table 2: Ablation study for the dome case study at the final rollout timestep.

Model	Displacement evaluation		Thinning evaluation	
	Mean positional Euclidean error (mm)	Position MAE (mm)	Threshold-based thinning error	Top 5% critical relative thinning error
MGN	0.82732	0.38660	0.00746	4.20%
RGNN	0.67450 (-18.5%)	0.31378 (-18.8%)	0.00614 (-17.8%)	3.12% (-25.8%)
Vanilla-BiGNN	0.90810 (+9.8%)	0.41662 (+7.8%)	0.00538 (-27.9%)	3.23% (-23.2%)
GAT-BiGNN	0.89938 (+8.70%)	0.42227 (+9.2%)	0.00571 (-23.5%)	3.40% (-18.6%)
CA-BiGNN	0.73513 (-11.1%)	0.34162 (-11.6%)	0.00532 (-28.7%)	2.96% (-29.5%)
CAtt-BiGNN (proposed)	0.64817 (-21.7%)	0.30762 (-20.4%)	0.00484 (-35.1%)	2.52% (-39.9%)

* Values in parentheses denote the relative change (%) with respect to the MGN baseline (lower is better).

model can adaptively weight element–node messages more effectively during aggregation.

Figure 9 presents the evolution of Euclidean positional error and threshold-based thinning error over the 10 rollout timesteps for the dome-shaped case study. The models show similar displacement errors during the early and intermediate rollout stages, while CAtt-BiGNN gives the lowest positional error in later-timesteps. For threshold-based thinning error, CAtt-BiGNN remains among the lowest-error models over most timesteps and gives the lowest error at the final timestep. These temporal trends are consistent with Table 2, where CAtt-BiGNN achieves the lowest final displacement errors and threshold-based thinning error among the compared models.

Figure 10 shows the visual comparison of predicted and ground-truth fields for the dome-shaped case study with the largest dome radius in the test set. The positional and thinning errors are evaluated at the final rollout timestep. Figure 10 provides a qualitative comparison of the final rollout predictions for the dome-shaped case. The node-centred baselines reproduce the overall shape but show visible error concentrations in regions with high curvature and geometric transition. Vanilla-BiGNN improves the thinning field

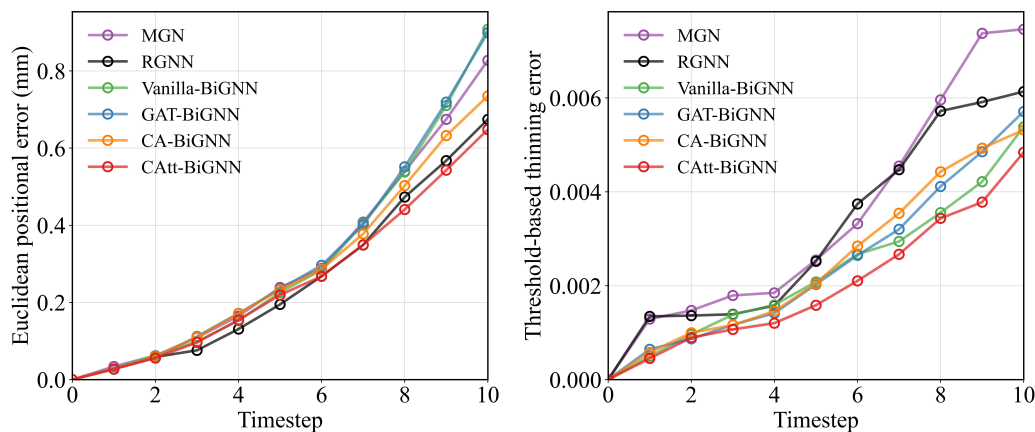


Figure 9: Dome case: evolution of test-set mean errors over the 10 autoregressive rollout transitions. (a) Euclidean positional error in mm. (b) Thresholded thinning error computed over elements whose FE reference thinning magnitude exceeds the selected threshold.

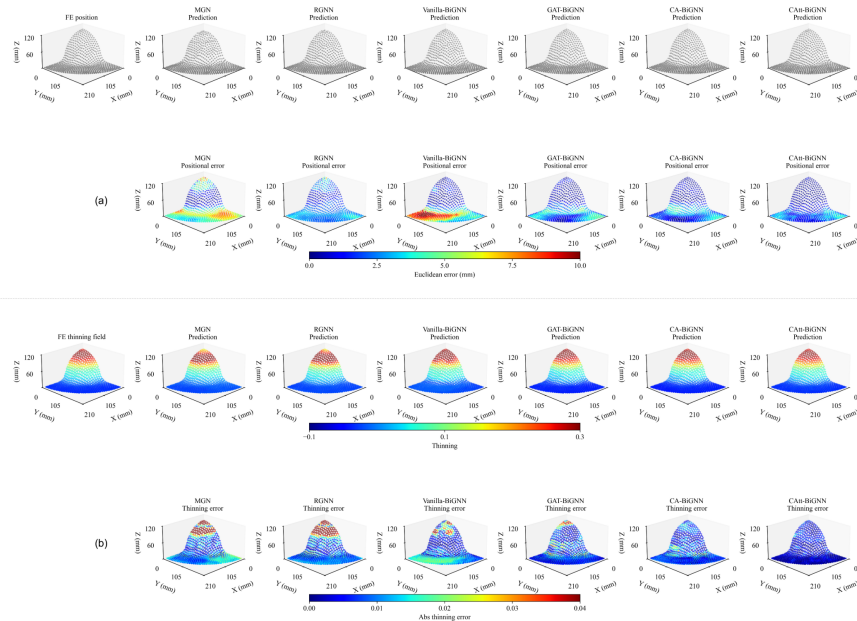


Figure 10: Final-timestep visual comparison for the dome test case with the largest dome radius in the test set. Columns show the FE reference and predictions from MGN, RGNN, Vanilla-BiGNN, GAT-BiGNN, CA-BiGNN, and CAtt-BiGNN. Panel (a) compares deformed nodal positions and Euclidean position-error maps. Panel (b) compares elemental thinning fields and absolute thinning-error maps. Colour bars indicate position error in mm and dimensionless thinning error.

in these regions. However, its displacement prediction remains less accurate. This suggests that the bipartite graph formulation reduces interpolation errors between nodes and elements. Nevertheless, the coupling between nodal and elemental states is not effectively learnt. Consequently, errors originating in one field tend to propagate to the other through the message-passing process. This behaviour is evident in the figure, where the high-error regions in the thinning and displacement fields for Vanilla-BiGNN exhibit similar spatial locations and patterns. The attention-based variants reduce some of these errors by assigning nonuniform weights to node-element interactions. Among them, CAtt-BiGNN gives the most balanced visual agreement with the FE reference across both displacement and thinning fields.

8.2. Corner-shaped case study

The corner-shaped case study involves larger graphs and sharper geometric transitions than the dome-shaped case. All models in this comparison therefore use a downsampling and upsampling mechanism, so the ablation focuses on how the bipartite representation and attention mechanism behave within a hierarchical graph architecture.

Baseline models. Six model configurations are evaluated: (a) UMGNN, which extends MeshGraphNet by incorporating a downsampling and upsampling mechanism. (b) RUGNN, which is UMGNN equipped with recurrent updates to better capture temporal dependencies [26]. (c) Vanilla-BiUGNN, our BiGNN variant that incorporates bipartite graph construction together with a hierarchical downsampling and upsampling mechanism, but without any attention-based aggregation functions. (d) GAT-BiUGNN, which extends Vanilla-BiUGNN with GAT-based attention aggregation. (e) CA-BiUGNN, which extends Vanilla-BiUGNN with cross-attention-based aggregation. (f) The proposed CAtt-BiUGNN model, which extends Vanilla-BiUGNN with the designed edge-based cross-attention aggregation, following the method introduced in Section 6.2.2. Specifically, the main difference between CA-BiUGNN and our proposed CAtt-BiUGNN is that CA-BiUGNN computes the Key matrix from source mesh node or element centre-node features, whereas CAtt-BiUGNN derives them from edge features.

Among these comparative models, UMGNN and RUGNN are treated as external baselines, while Vanilla-BiUGNN, GAT-BiUGNN, and CA-BiUGNN represent the ablation variants. All models use the recommended hyperpa-

rameters and the same GPU setup described in Section 7.1. Table 3 summarises the results.

Evaluation metrics. The evaluation metrics are designed to examine whether the proposed nodal-elemental representation and edge-aware cross-attention processor improve autoregressive prediction of manufacturability-oriented fields. Positional metrics assess the predicted geometry evolution, while thinning-based metrics assess element-level deformation accuracy, and prediction accuracy in thinning-critical regions. Each simulation consists of ten rollout timesteps. Similar to the dome-shaped case study, dual outputs are produced, namely displacement fields at the nodal level and thinning fields at the element level. The evaluation metrics follow those used for the dome-shaped case study in Section 8.1.

Results. Table 3 reports the final-timestep results for the corner-shaped case study. All relative changes are computed with respect to UMGN. Compared with UMGN, Vanilla-BiUGNN substantially improves the thinning metrics and also reduces the displacement errors. However, Vanilla-BiUGNN remains less accurate than RUGNN on the displacement metrics, showing that the hierarchical bipartite representation still requires an effective coupling mechanism to update nodal states robustly.

GAT-BiUGNN slightly improves the thinning-related metrics over Vanilla-BiUGNN, but does not improve the displacement metrics. This indicates that GAT-style self-attention is less effective for modelling the asymmetric and directional interactions between mesh nodes and element centre-nodes in a bipartite graph structure. CA-BiUGNN improves over GAT-BiUGNN on displacement metrics and threshold-based thinning error, but its performance is comparable to the Vanilla-BiUGNN model. This may suggest that CA-BiUGNN does not fully capture the coupling required to update nodal displacements. Because CA-BiUGNN constructs the key and value representations from source mesh node or element centre-node features, its attention weights are less directly conditioned on the directed node–element edge geometry. This may limit its ability to distinguish local geometric relations that are important for coupled displacement–thinning prediction.

CAtt-BiUGNN achieves the overall best performance, reducing the mean positional Euclidean error by 41.9%, position MAE by 41.1%, thresholded thinning error by 73.8%, and top-1% relative thinning error by 86.4% relative to UMGN. These results support the edge-aware attention design in the hierarchical setting. In the corner case, deformation depends strongly on local

Table 3: Ablation study for the corner case study at the final rollout timestep.

Model	Displacement evaluation		Thinning evaluation	
	Mean positional Euclidean error (mm)	Position MAE (mm)	Threshold-based thinning error	Top 1% critical relative thinning error
UMGN	3.15071	1.29060	0.01038	35.87%
RUGNN	2.04148	0.89816	0.00541	19.59%
	(-35.2%)	(-30.4%)	(-47.9%)	(-45.4%)
Vanilla- BiUGNN	2.17344	0.91474	0.00334	6.74%
	(-31.0%)	(-29.1%)	(-67.9%)	(-81.2%)
GAT-BiUGNN	2.33186	0.94718	0.00305	5.96%
	(-26.0%)	(-26.6%)	(-70.7%)	(-83.4%)
CA-BiUGNN	2.20014	0.90191	0.00291	7.87%
	(-30.2%)	(-30.1%)	(-72.0%)	(-78.1%)
CAtt-BiUGNN (proposed)	1.83203	0.75597	0.00272	4.89%
	(-41.9%)	(-41.1%)	(-73.8%)	(-86.4%)

* Values in parentheses denote the relative change (%) with respect to the UMGNN baseline (lower is better).

geometric relations around the corner radius and contact regions. By deriving attention information from directed edge features, CAtt-BiUGNN can modulate node-element messages using these local geometric cues. This helps the model combine element-level thinning prediction with accurate nodal displacement prediction over a larger graph.

To examine whether the improved accuracy is mainly attributable to the number of trainable parameters, an additional parameter-budget-controlled comparison is provided in Appendix E. In this comparison, the hidden dimensions of UMGNN and RUGNN are adjusted from 128 to 212, yielding trainable-parameter counts comparable to those of the BiUGNN variants. This comparison is not intended as an exhaustive hyperparameter search, but as a controlled parameter-budget check. The UMGNN-212 and RUGNN-212 variants improve some metrics relative to their 128-dimensional counterparts, but CAtt-BiUGNN remains the best-performing model under a comparable trainable-parameter budget. These results indicate that increasing the trainable-parameter budget alone does not fully explain the performance difference. The remaining improvement is therefore likely related to the proposed bipartite node–element representation and edge-aware coupling design.

Figure 11 presents the evolution of the Euclidean positional error and threshold-based thinning error over the 10 rollout timesteps for the corner-shaped case study. CAtt-BiUGNN achieves the lowest final-timestep error for both metrics and generally remains among the best-performing models across the rollout. Its error trajectory is also lower than those of the node-centred hierarchical baselines, UMGN and RUGNN, over most timesteps. Compared with the other bipartite variants, the advantage of CAtt-BiUGNN is more evident in the later rollout stages, particularly for the threshold-based thinning error. These trends are consistent with Table 3, where CAtt-BiUGNN achieves the lowest final displacement errors and threshold-based thinning error among the compared models.

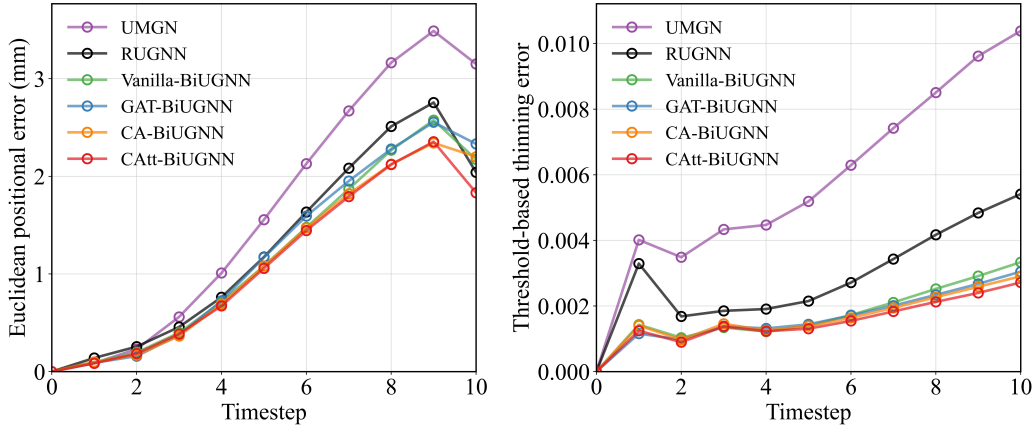


Figure 11: Corner case: evolution of test-set mean errors over the 10 autoregressive rollout transitions. (a) Euclidean positional error in mm. (b) Thresholded thinning error computed over elements whose FE reference thinning magnitude exceeds the selected threshold.

Figure 12 shows the final rollout predictions for a corner-shaped test case with the largest height value in the test set. This case is used to visualise model behaviour under a relatively pronounced geometric configuration, where the corner region and contact-driven deformation are of particular interest. The hierarchical node-centred baselines, MGN and RUGNN, capture the global shape but show larger errors around the corner radius and high-curvature regions. Vanilla-BiUGNN reduces the element-level thinning error by representing thinning on element centre-nodes, although displacement errors remain visible near the deformed corner region. The attention-based variants improve the spatial distribution of the predicted fields by weighting node-element interactions nonuniformly. Among them, CAtt-BiUGNN

shows close visual agreement with the FE reference across both displacement and thinning fields, particularly around the corner and contact-driven deformation regions. This visual comparison is consistent with Table 3, where CAtt-BiUGNN achieves the lowest final displacement and threshold-based thinning errors.

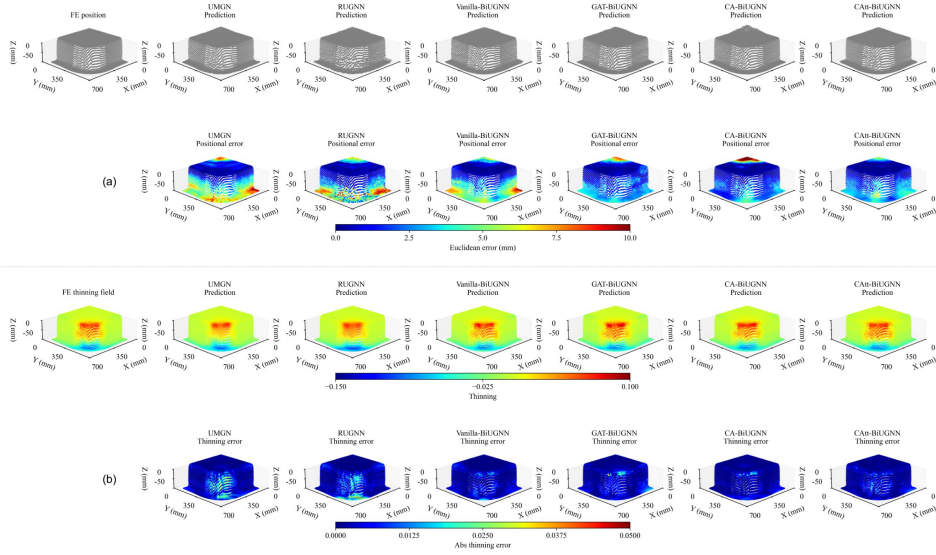


Figure 12: Final-timestep visual comparison for a corner test case with the highest height value in the test set. Columns show the FE reference and predictions from UMGNN, RUGNN, Vanilla-BiUGNN, GAT-BiUGNN, CA-BiUGNN, and CAtt-BiUGNN. Panel (a) compares deformed nodal positions and Euclidean position-error maps. Panel (b) compares elemental thinning fields and absolute thinning-error maps. Colour bars indicate position error in mm and dimensionless thinning error.

Figure 13 shows the node-to-element attention weights computed at the final processor layer of the trained CAtt-BiUGNN model. The results are compared against those from the GAT-BiUGNN and CA-BiUGNN models.

Figure 13 visualises the deviation of the learned node-to-element attention weights from uniform mean aggregation. For an element centre-node i , the uniform attention weight is $1/|\mathcal{N}(i)|$, where $\mathcal{N}(i)$ denotes the set of mesh nodes connected to element centre-node i . The plotted quantity is therefore

$$\Delta\alpha_{v \rightarrow i, L}^{N_p} = \alpha_{v \rightarrow i, L}^{N_p} - \frac{1}{|\mathcal{N}(i)|}. \quad (52)$$

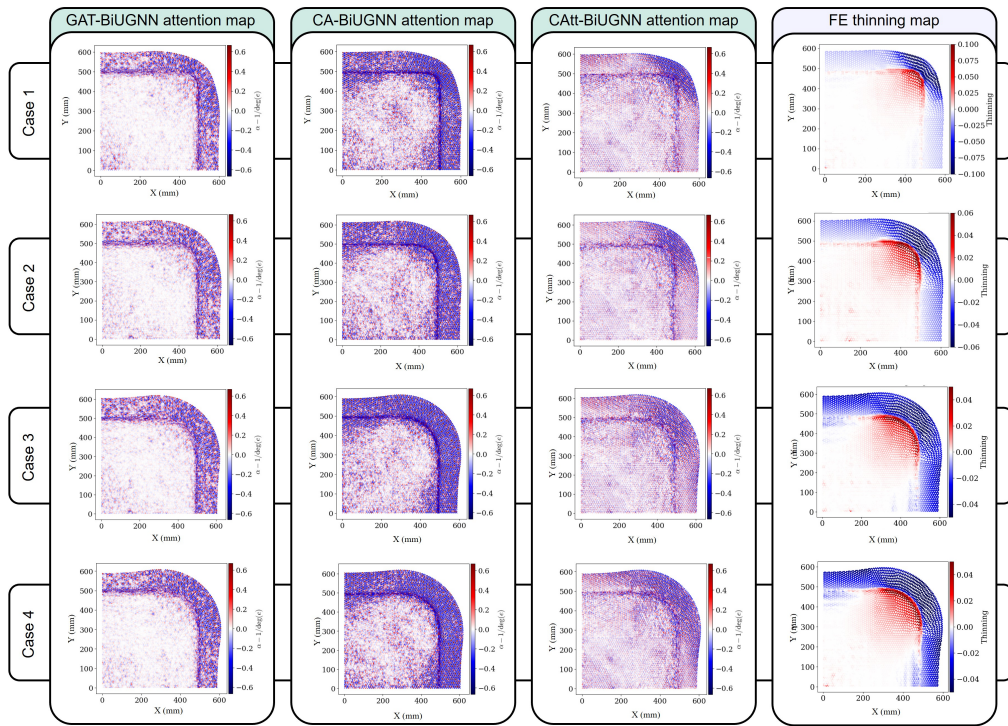


Figure 13: Attention-deviation maps for the corner-shaped test cases at the final rollout timestep. Each row shows one representative test case. The first three columns compare the node-to-element attention deviation maps of GAT-BiUGNN, CA-BiUGNN, and CAtt-BiUGNN, respectively. The last column shows the corresponding FE thinning field as a spatial reference. Positive and negative deviations indicate messages weighted above and below uniform aggregation, respectively.

Positive values indicate node-to-element edges receiving greater weight than uniform aggregation, whereas negative values indicate suppressed edges.

The GAT-BiUGNN and CA-BiUGNN maps show relatively weak case-to-case variation, which is consistent with the limited improvement compared to Vanilla-BiUGNN in Table 3. CAtt-BiUGNN produces more spatially structured attention patterns near geometric transitions and thinning-prone regions. These maps should be interpreted as qualitative evidence that edge-aware attention adapts to local node–element geometry, rather than as evidence that the network explicitly enforces finite-element equilibrium or physical consistency. This interpretation helps explain why edge-aware message weighting improves the overall predictive balance between nodal displacement and elemental thinning.

8.3. Comparison of different noise strategies

The noise-ablation study is separated from the baseline architecture comparison for two related reasons. First, in this implementation, the perturbation is introduced only through the nodal displacement-increment input. Its effect is therefore expected to be most direct on displacement rollout, whereas its influence on elemental thinning prediction is indirect, because thinning is predicted on element centre-nodes and is affected through the learned node–element coupling during rollout. Second, the appropriate noise perturbation form and scale may depend on the model architecture. Applying independently tuned noise settings to different baselines would make it difficult to distinguish architectural effects from noise-strategy tuning. Note that the baseline architecture comparison results in Section 8.1 and Section 8.2 are conducted under the common noise-free training setting. The adaptive Gaussian noise strategy is therefore analysed separately as an optional rollout-stabilisation technique for the proposed architecture.

Based on this separation, the noise-ablation experiment is conducted on the corner-shaped case study using CAtt-BiUGNN as the reference architecture. The CAtt-BiUGNN without noise corresponds to the proposed architecture reported in the baseline comparison in Section 8.2. Three settings are compared: CAtt-BiUGNN without noise, CAtt-BiUGNN with uniform Gaussian noise, and CAtt-BiUGNN with the adaptive Gaussian noise strategy described in Section 7.2. The architecture, training dataset, and evaluation protocol are kept unchanged, and only the training perturbation strategy is varied. For the two noise-injection settings, the noise scale is selected using validation experiments only; the test set is not used for selecting noise

Table 4: Noise-ablation study for CAtt-BiUGNN on the corner case at the final rollout timestep.

Training setting	Displacement evaluation		Thinning evaluation	
	Mean positional Euclidean error (mm)	Position MAE (mm)	Threshold-based thinning error	Top 1% critical relative thinning error
CAtt-BiUGNN without noise	1.83203	0.75597	0.00272	4.89%
CAtt-BiUGNN with uniform Gaussian noise	0.47951 (-73.8%)	0.22195 (-70.6%)	0.00231 (-15.1%)	4.39% (-10.1%)
CAtt-BiUGNN with adaptive Gaussian noise	0.47078 (-74.3%)	0.21366 (-71.7%)	0.00197 (-27.6%)	3.69% (-24.4%)

* Values in parentheses denote the relative change (%) with respect to CAtt-BiUGNN trained without noise (lower is better).

parameters. The results are reported in Table 4.

Table 4 evaluates noise injection as a rollout-stabilisation strategy for the corner-shaped case. Since the perturbation is introduced through the nodal displacement-increment input, the largest error reduction is observed in the displacement-based metrics. Its influence on elemental thinning metrics is less direct, because thinning is predicted on element centre-nodes and is mediated by the learned node–element coupling during rollout. The adaptive strategy gives a more balanced improvement across displacement and thinning-related metrics, although the improvement in thinning localisation remains smaller than that in displacement prediction.

Based on this ablation, the adaptive Gaussian noise strategy is adopted for the final qualitative rollout visualisations presented in the appendices. Note that the baseline comparisons in the main results tables in Section 8.1 and Section 8.2 are conducted under the noise-free setting, so that the architectural effects can be evaluated without the additional influence of noise injection. The prediction results for additional dome test cases are presented in Appendix A, and the corresponding temporal rollout predictions are shown in Appendix B. The prediction results on different test sets for the corner case study are illustrated in Appendix C, and the temporal rollout prediction results are shown in Appendix D. These appendices show that, under the

adaptive-noise training strategy, the predictions of CAtt-BiUGNN remain closely aligned with the FE simulation results across different geometries and rollout timesteps.

9. Conclusion

This study proposed CAtt-BiGNN, a cross-attention-based bipartite graph neural network for coupled nodal and elemental field prediction in large-deformation sheet material forming. The work was motivated by the observation that explicit dynamic FE simulations involve coupled updates between nodal kinematics and element-level deformation measures, while many mesh based graph surrogates represent the evolving graph state primarily on mesh nodes. The proposed bipartite graph representation retains mesh nodes and finite elements as distinct but coupled graph entities. This allows nodal displacement increments and element-level deformation states to be predicted on their native discretisation domains. In the sheet-forming instantiation considered in this work, the element-level state corresponds to elemental thinning. The model remains a learned simulator rather than an explicitly constrained FE solver, but the representation provides a finite-element-inspired inductive bias for learning nodal-elemental interactions from simulation data.

The proposed edge-aware cross-attention processor further improves the modelling of directional node-element coupling. This allows the message-passing weights to depend on local geometric relations between mesh nodes and finite elements. For large forming graphs, the hierarchical CAtt-BiUGNN extension combines the same bipartite processor with a graph downsampling and upsampling mechanism, enabling longer-range information propagation while preserving the nodal-elemental representation across graph levels.

The numerical results support the proposed modelling choices. In the dome-shaped benchmark, CAtt-BiGNN improves the overall balance between nodal displacement prediction and elemental thinning prediction relative to mesh based node-centred baselines and bipartite ablation variants. In the corner-shaped benchmark, which involves a larger graph, sharper geometric transitions, and more complex hot-forming conditions, CAtt-BiUGNN provides the strongest overall performance among the evaluated hierarchical architectures. The ablation results further show that the performance gain is not due to the bipartite representation alone, but also to the proposed edge-aware node-element coupling and hierarchical propagation. The adaptive Gaussian noise strategy is evaluated separately as an optional rollout-

stabilisation technique, and the results indicate that it can further improve robustness in the corner-forming case.

Overall, the proposed framework provides a finite-element-inspired graph learned simulator for predicting manufacturability-oriented nodal and elemental fields during autoregressive rollout. The present evaluation focuses on geometry-driven generalisation within two sheet-forming benchmark families under fixed material and process settings. Future work will extend the graph state and dataset construction to include richer element-level variables, material descriptors, process parameters, contact conditions, and mesh-topology variations. Integrating the learned simulator into optimisation workflows may further support rapid manufacturability assessment and efficient design-space exploration in large-deformation forming analysis.

Acknowledgement

The authors acknowledge funding support from UKRI (UKRI221: AI-Driven Design for Forming High-Performance Vehicle Parts), as well as PhD scholarships from Imperial College London. The authors would like to thank ESI Group for their technical support with the PAM-STAMP software. For the purpose of open access, the authors have applied a Creative Commons Attribution (CC BY) license to any Author Accepted Manuscript version arising.

CRedit authorship contribution statement

Yingxue Zhao: Conceptualization, Methodology, Software, Investigation, Data curation, Formal analysis, Validation, Visualization, Writing – original draft, Writing – review & editing. **Haoran Li:** Methodology, Formal analysis, Validation, Writing – review & editing. **Haosu Zhou:** Methodology, Formal analysis, Writing – review & editing. **Tobias Pfaff:** Methodology, Validation, Supervision, Writing – review & editing. **Nan Li:** Conceptualization, Methodology, Formal analysis, Validation, Supervision, Project administration, Funding acquisition, Writing – review & editing.

Declaration of competing interest

The authors declare that they have no known competing financial interests or personal relationships that could have appeared to influence the work reported in this paper.

Data availability

The data supporting the findings of this study are available upon reasonable request.

Appendix A. Prediction results on dome-shaped case study

Figure A.14 presents the prediction performance of the adaptive-noise variant of CAtt-BiGNN. Three representative dome-shaped cases, corresponding to the smallest, median, and largest dome radii within the design space, are displayed. Across all three cases, the predicted geometries are in close agreement with the FE simulation results, with Euclidean positional errors at the final timestep remaining below approximately 5 mm. The predicted thinning fields also exhibit a high level of consistency with the FE ground truth, capturing the spatial variation of the thinning field with strong fidelity. These results suggest that the model maintains reliable predictive accuracy across dome geometries with substantially different curvature conditions.

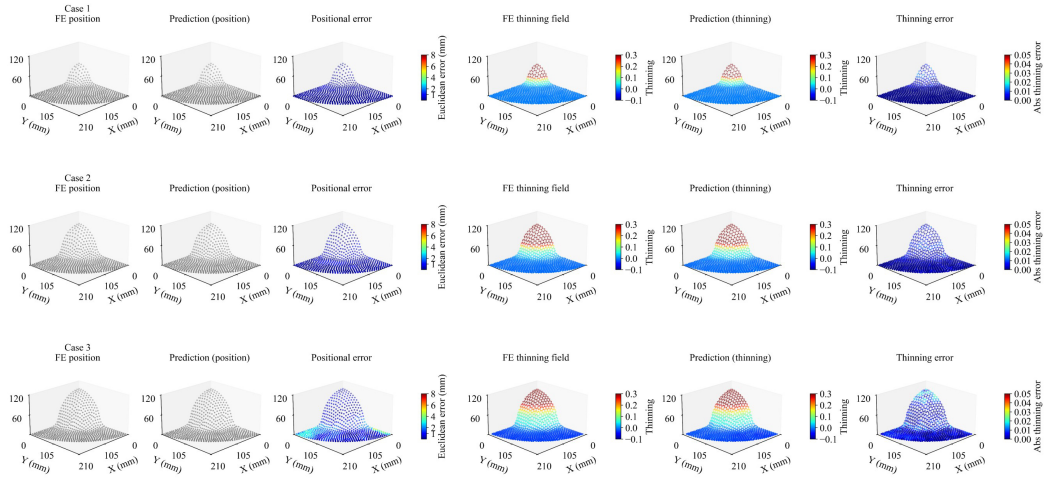


Figure A.14: Final-timestep predictions of the adaptive-noise CAtt-BiGNN variant for three dome test cases. Each row corresponds to one design case. Columns show FE reference position, predicted position, Euclidean position error, FE thinning field, predicted thinning field, and absolute thinning error.

Appendix B. Temporal rollout prediction results on dome-shaped case study

Figure B.15 illustrates the temporal rollout performance of the adaptive-noise CAtt-BiGNN variant. Two dome-shaped cases, corresponding to the smallest and largest dome radii, are displayed. The results show that the model produces temporally coherent and stable predictions throughout the rollout sequence. The deformation and thinning fields evolve smoothly over time and remain closely aligned with the FE simulation results across all timesteps. The differences between the predicted and ground-truth thinning fields are minor, indicating that the model can effectively maintain its predictive accuracy during autoregressive rollout without severe error accumulation.

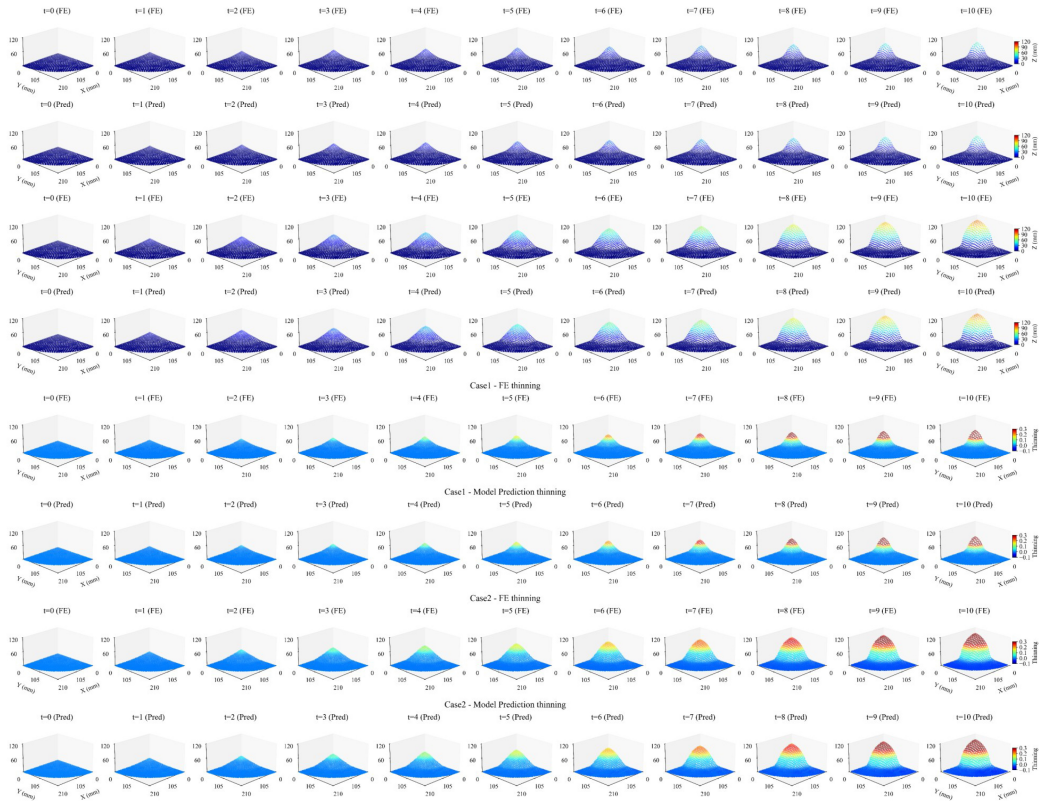


Figure B.15: Temporal rollout predictions of the adaptive-noise CAtt-BiGNN variant for two dome test cases. Columns correspond to rollout timesteps. Rows compare FE and predicted deformed positions for each case, followed by FE and predicted thinning fields. The figure illustrates temporal consistency during autoregressive rollout.

Appendix C. Prediction results on corner-shaped case study

Figure C.16 presents the prediction performance of the adaptive-noise CAtt-BiUGNN variant. Three representative cases situated at the boundaries of the design space are displayed. These cases were selected to assess the model’s performance under the smallest and largest combinations of height and planar radius.

Across all cases, the predicted geometries closely match the FE-simulated shapes, with Euclidean positional errors remaining below approximately 2.5 mm. The predicted thinning fields are also highly consistent with the FE ground truth, and the corresponding error maps show absolute error values mostly

below 0.03. These visual results indicate that the model maintains strong predictive accuracy across a wide range of geometric variations.

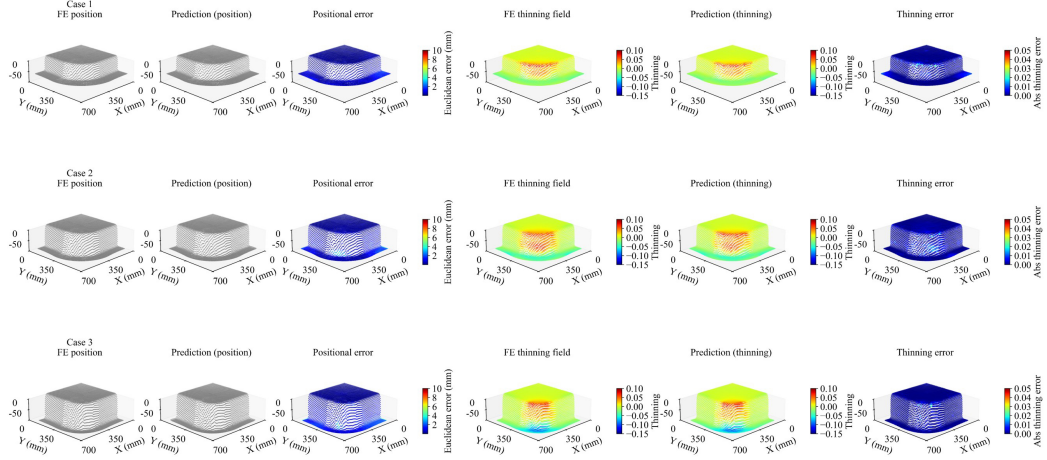


Figure C.16: Final-timestep predictions of the adaptive-noise CAtt-BiUGNN variant for three corner test cases. Each row corresponds to one design case. Columns show FE reference position, predicted position, Euclidean position error, FE thinning field, predicted thinning field, and absolute thinning error.

Appendix D. Temporal rollout prediction results on corner-shaped case study

Figure D.17 illustrates the temporal rollout performance of the adaptive-noise CAtt-BiUGNN variant. Two representative test cases, consistent with those in Appendix C, are selected to assess the stability and accuracy of the model’s autoregressive predictions. The visualisations show the evolution of the predicted deformation and thinning fields from the initial to the final timestep.

The predicted sequences exhibit smooth and realistic temporal transitions that align closely with the FE results. The differences between the predicted and ground-truth thinning fields remain small throughout the rollout, demonstrating that the model preserves high accuracy across all timesteps without error accumulation.

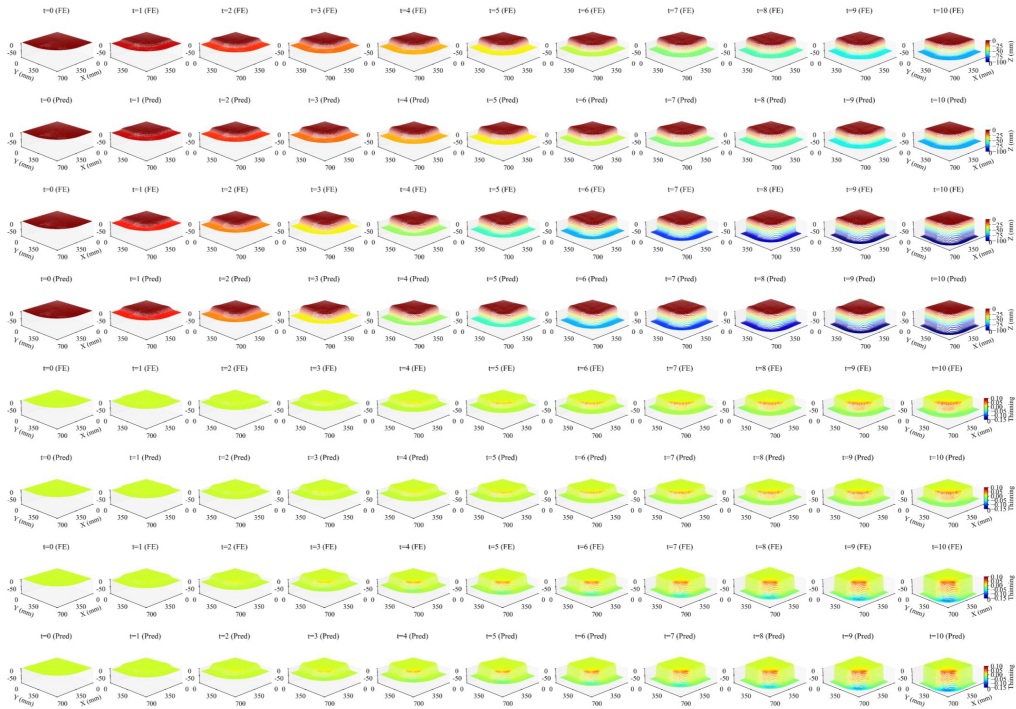


Figure D.17: Temporal rollout predictions of the adaptive-noise CAtt-BiUGNN variant for two corner test cases. Columns correspond to rollout timesteps. Rows compare FE and predicted deformed positions for each case, followed by FE and predicted thinning fields. The figure illustrates the stability of autoregressive predictions across the forming process.

Appendix E. Parameter-budget-controlled comparison

This appendix provides the parameter-budget-controlled comparison referred to in Section 8.2. The comparison is included to examine whether the relative performance of the models changes when the trainable-parameter counts of the baseline models are made comparable to those of the BiUGNN variants.

Table E.5 reports the corresponding results. Increasing the hidden dimension affects UMGN and RUGNN differently across the displacement and thinning metrics. UMGN-212 improves the positional Euclidean error and position MAE relative to UMGN-128, but does not improve the threshold-based thinning error or the top-1% critical relative thinning error. RUGNN-212 improves most of the reported metrics relative to RUGNN-128, except for

Table E.5: Parameter-budget-controlled comparison.

Model	Displacement evaluation		Thinning evaluation		Model size
	Mean positional Euclidean error (mm)	Position MAE (mm)	Threshold-based thinning error	Top 1% critical relative thinning error	Total trainable parameters
UMGN-128	3.15071	1.29060	0.01038	35.87%	82,917,604
UMGN-212	2.29230	1.00081	0.01070	37.09%	227,439,646
RUGNN-128	2.04148	0.89816	0.00541	19.59%	85,268,708
RUGNN-212	2.04876	0.85130	0.00444	17.20%	233,866,850
Vanilla-BiUGNN	2.17344	0.91474	0.00334	6.74%	237,289,988
GAT-BiUGNN	2.33186	0.94718	0.00305	5.96%	237,630,112
CA-BiUGNN	2.20014	0.90191	0.00291	7.87%	239,322,116
CAtt-BiUGNN	1.83203	0.75597	0.00272	4.89%	239,490,052

the positional Euclidean error. Among the bipartite attention-based variants, GAT-BiUGNN and CA-BiUGNN improve some metrics relative to Vanilla-BiUGNN, while CAtt-BiUGNN gives lower errors in both displacement and thinning evaluation metrics.

References

- [1] T. J. R. Hughes, The Finite Element Method: Linear Static and Dynamic Finite Element Analysis, Prentice-Hall, Englewood Cliffs, NJ, 1987.
- [2] K. Bathe, Finite Element Procedures, Prentice Hall, 2006.
URL <https://books.google.co.uk/books?id=rWvefGICf08C>
- [3] T. Belytschko, W. K. Liu, B. Moran, K. Elkhodary, Nonlinear finite elements for continua and structures, John wiley & sons, 2014.
- [4] D. Politis, A. Foster, N. Li, L. Wang, J. Lin, A. Foster, D. Szegda, Prediction of thinning behavior for complex-shaped, lightweight alloy panels formed through a hot stamping process, in: Advanced High Strength

Steel and Press Hardening: Proceedings of the 2nd International Conference (ICHSU2015), World Scientific, 2016, pp. 395–401.

- [5] Z. Marciniak, J. L. Duncan, S. J. Hu, *Mechanics of Sheet Metal Forming*, Butterworth-Heinemann, Great Britain, 2002.
- [6] Y. Fei, S. Qin, W. Liao, H. Guan, X. Lu, Graph neural network-assisted evolutionary algorithm for rapid optimization design of shear-wall structures, *Advanced Engineering Informatics* 65 (2025) 103129. doi:10.1016/j.aei.2025.103129.
- [7] J. Kim, T. Park, S. Cho, J. Park, G. Noh, Maestro: a multi-fidelity modeling assisted by an ensemble of surrogates for robust prediction, *Advanced Engineering Informatics* 76 (2025) 104889. doi:10.1016/j.aei.2026.104889.
- [8] H. R. Attar, H. Zhou, A. Foster, N. Li, Rapid feasibility assessment of components to be formed through hot stamping: A deep learning approach, *Journal of Manufacturing Processes* 68 (2021) 1650–1671. doi:https://doi.org/10.1016/j.jmapro.2021.06.011.
- [9] H. Zhou, H. Li, Y. Zhao, P. R. Childs, N. Li, Image-based artificial intelligence-driven modelling for blank shape optimisation in sheet metal forming, *Materials & Design* (2025) 114302.
- [10] J. Willard, X. Jia, S. Xu, M. Steinbach, V. Kumar, Integrating physics-based modeling with machine learning: A survey (03 2020). doi:10.48550/arXiv.2003.04919.
- [11] G. E. Karniadakis, I. G. Kevrekidis, L. Lu, P. Perdikaris, S. Wang, L. Yang, Physics-informed machine learning, *Nature Reviews Physics* 3 (2021) 422–440. doi:10.1038/s42254-021-00314-5.
- [12] V. K. Dubey, C. E. Haese, O. Gültekin, D. Dalton, M. K. Rausch, J. Fuhs, Graph neural network surrogates for contacting deformable bodies with necessary and sufficient contact detection, *Computer Methods in Applied Mechanics and Engineering* 448 (2026) 118413. doi:https://doi.org/10.1016/j.cma.2025.118413.

- [13] L. Xing, P. Gardoni, G. Song, Y. Zhou, Deep learning-based surrogate capacity models and multi-objective fragility estimates for reinforced concrete frames, *Computer Methods in Applied Mechanics and Engineering* 440 (2025) 117928. doi:<https://doi.org/10.1016/j.cma.2025.117928>.
- [14] H. Attar, H. Zhou, N. Li, Deformation and thinning field prediction for hfq® formed panel components using convolutional neural networks, *IOP Conference Series: Materials Science and Engineering* 1157 (2021) 012079. doi:10.1088/1757-899X/1157/1/012079.
- [15] P. W. Battaglia, J. B. Hamrick, V. Bapst, A. Sanchez-Gonzalez, V. Zambaldi, M. Malinowski, A. Tacchetti, D. Raposo, A. Santoro, R. Faulkner, et al., Relational inductive biases, deep learning, and graph networks, *arXiv preprint arXiv:1806.01261* (2018).
- [16] J. Gilmer, S. S. Schoenholz, P. F. Riley, O. Vinyals, G. E. Dahl, Neural message passing for quantum chemistry, in: *International conference on machine learning*, Pmlr, 2017, pp. 1263–1272.
- [17] Z. Wu, S. Pan, F. Chen, G. Long, C. Zhang, P. S. Yu, A comprehensive survey on graph neural networks, *IEEE transactions on neural networks and learning systems* 32 (1) (2020) 4–24.
- [18] A. Sanchez-Gonzalez, J. Godwin, T. Pfaff, R. Ying, J. Leskovec, P. Battaglia, Learning to simulate complex physics with graph networks, in: *International conference on machine learning*, PMLR, 2020, pp. 8459–8468.
- [19] T. Pfaff, A. Sanchez-Gonzalez, P. W. Battaglia, et al., Learning mesh-based simulation with graph neural networks, *International Conference on Learning Representations* (2021).
- [20] M. M. Bronstein, J. Bruna, T. Cohen, P. Veličković, Geometric deep learning: Grids, groups, graphs, geodesics, and gauges, *arXiv preprint arXiv:2104.13478* (2021).
- [21] A. Sanchez-Gonzalez, N. Heess, J. T. Springenberg, J. Merel, M. Riedmiller, R. Hadsell, P. Battaglia, Graph networks as learnable physics engines for inference and control, in: *International conference on machine learning*, PMLR, 2018, pp. 4470–4479.

- [22] P. Battaglia, R. Pascanu, M. Lai, D. Jimenez Rezende, et al., Interaction networks for learning about objects, relations and physics, *Advances in neural information processing systems* 29 (2016).
- [23] D. Dalton, D. Husmeier, H. Gao, Physics-informed graph neural network emulation of soft-tissue mechanics, *Computer Methods in Applied Mechanics and Engineering* 417 (2023) 116351.
- [24] L. Patrignani, S. T. Pinho, Graph neural networks with hybrid local-global attention for effective prediction of mechanical response in structures, *Computer Methods in Applied Mechanics and Engineering* 452 (2026) 118753. doi:<https://doi.org/10.1016/j.cma.2026.118753>.
- [25] Y. Zhao, H. Li, H. Zhou, H. R. Attar, T. Pfaff, N. Li, A review of graph neural network applications in mechanics-related domains, *Artificial Intelligence Review* 57 (11) (2024) 315.
- [26] Y. Zhao, Q. Chen, H. Li, H. Zhou, H. R. Attar, T. Pfaff, T. Wu, N. Li, Recurrent u-net-based graph neural network (rugnn) for accurate deformation predictions in sheet material forming, *Advanced Engineering Informatics* 69 (2026) 104021.
- [27] Y. Zhao, H. Li, H. Zhou, H. R. Attar, T. Pfaff, N. Li, Rapid prediction of material deformation in hot stamping of battery box geometries using graph neural network, in: *Journal of Physics: Conference Series*, Vol. 3104, IOP Publishing, 2025, p. 012057.
- [28] Q. Chen, J. Cao, W. Lin, S. Zhu, S. Wang, Predicting dynamic responses of continuous deformable bodies: A graph-based learning approach, *Computer Methods in Applied Mechanics and Engineering* 420 (2024) 116669.
- [29] N. Black, A. R. Najafi, Learning finite element convergence with the multi-fidelity graph neural network, *Computer Methods in Applied Mechanics and Engineering* 397 (2022) 115120.
- [30] K. Zheng, D. J. Politis, L. Wang, J. Lin, A review on forming techniques for manufacturing lightweight complex—shaped aluminium panel components, *International Journal of Lightweight Materials and Manufacture* 1 (2) (2018) 55–80.

- [31] K. Zheng, J. Lee, D. J. Politis, N. Li, J. Lin, T. A. Dean, An analytical investigation on the wrinkling of aluminium alloys during stamping using macro-scale structural tooling surfaces, *The International Journal of Advanced Manufacturing Technology* 92 (1) (2017) 481–495.
- [32] N. Li, C. Sun, N. Guo, M. Momhamed, J. Lin, M. Takeki, Damage investigation of boron steel at hot stamping conditions, *Procedia Engineering* 81 (2014) 1744–1749.
- [33] X. Fu, F. Zhou, D. Peddireddy, Z. Kang, M. B.-G. Jun, V. Aggarwal, An finite element analysis surrogate model with boundary oriented graph embedding approach for rapid design, *Journal of Computational Design and Engineering* 10 (3) (2023) 1026–1046.
- [34] H. Zhou, Y. Zhao, H. Li, T. Pfaff, N. Li, A multi-level graph-based surrogate model for real-time high-fidelity sheet forming simulations, *Advanced Engineering Informatics* 66 (2025) 103458.
- [35] S. Deshpande, S. Bordas, J. Lengiewicz, Magnet: A graph u-net architecture for mesh-based simulations, *arXiv preprint arXiv:2211.00713* (2022).
- [36] Z. He, T. Huang, B. Chen, Physics-informed graph transformer network for predicting cable-stayed bridge structural deflection response, *Advanced Engineering Informatics* 69 (2026) 103897. doi:10.1016/j.aei.2025.103897.
- [37] L. Bleker, K. M. M. Tam, P. D’Acunto, Logic-informed graph neural networks for structural form-finding, *Advanced Engineering Informatics* 61 (2024) 102510. doi:10.1016/j.aei.2024.102510.
- [38] T. Li, S. Zou, X. Chang, L. Zhang, X. Deng, Finite volume graph network (fvgn): Predicting unsteady incompressible fluid dynamics with finite volume informed neural network, *arXiv preprint arXiv:2309.10050* (2023).
- [39] R. Gao, I. K. Deo, R. K. Jaiman, A finite element-inspired hypergraph neural network: Application to fluid dynamics simulations, *Journal of Computational Physics* 504 (2024) 112866. doi:<https://doi.org/10.1016/j.jcp.2024.112866>.

- [40] Dassault Systèmes, United States of America, Getting Started with Abaqus Interactive Edition (2008).
- [41] W. Hosford, R. Caddell, Metal Forming: Mechanics and Metallurgy, Cambridge University Press, 2011.
URL <https://books.google.co.uk/books?id=x0GWAd7hNy0C>
- [42] B. Liang, S. Gao, W. Zhang, An integrated preforming-performance model for high-fidelity performance analysis of cured woven composite part with non-orthogonal yarn angles, Chinese Journal of Aeronautics 35 (6) (2022) 367–378.
- [43] M. Mohamed, N. Li, L. Wang, O. E. Fakir, J. Lin, T. Dean, J. Dear, An investigation of a new 2d cdm model in predicting failure in hfqing of an automotive panel, in: 4th International Conference on New Forming Technology (ICNFT 2015), EDP Sciences, 2015, p. 05011.